TECTONICS, VOL. 32, 540–557, doi:10.1002/tect.20020, 2013

Metamorphic field gradients across the Himachal Himalaya, northwest India: Implications for the emplacement of the Himalayan crystalline core

Remington M. Leger,[1,2] A. Alexander G. Webb,[1] Darrell J. Henry,[1] John A. Craig,[1] and Prashant Dubey[3]

Received 28 August 2012; revised 23 January 2013; accepted 3 February 2013; published 31 May 2013.

[1] New constraints on pressures and temperatures experienced by rocks of the Himachal Himalaya are presented in order to test models for the emplacement of the Himalayan crystalline core here. A variety of methods were employed: petrographic analysis referenced to a petrogenetic grid, exchange and net-transfer thermobarometry, Ti-in-biotite thermometry, and analysis of quartz recrystallization textures. Rocks along three transects (the northern Beas, Pabbar, and southern Beas transects) were investigated. Results reveal spatially coherent metamorphic field gradients across amphibolite-grade and migmatitic metamorphic rocks. Along the northern Beas transect, rocks record peak temperatures of ~650–780°C at low elevations to the north of ~32° 10' N; rocks in other structural positions along this transect record peak temperatures of <640°C that decrease with increasing structural elevation. Rocks of the Pabbar transect dominantly record ~650–700°C peak temperatures to the east of ~77° 55' E and ~450–620°C peak temperatures farther west. Peak temperatures of ~450–600°C along the southern Beas transect record a right-way-up metamorphic field gradient. Results are integrated with literature data to determine a metamorphic isograd map of the Himachal Himalaya. This map is compared to metamorphic isograd map pattern predictions of different models for Himalayan crystalline core emplacement. This analysis excludes models involving large magnitude (>20–30 km) extrusion and permits (1) models involving small magnitude (<20–30 km) extrusion that is discontinuous along the orogen and (2) tectonic wedging models, in which the crystalline core was emplaced at depth between a sole thrust and a back thrust in the Early-Middle Miocene.

Citation: Leger, R. M., A. A. G. Webb, D. J. Henry, J. A. Craig, and P. Dubey (2013), Metamorphic field gradients across the Himachal Himalaya, northwest India: Implications for the emplacement of the Himalayan crystalline core, *Tectonics*, *32*, 540–557, doi:10.1002/tect.20020.

1. Introduction

[2] First-order aspects of Himalayan tectonics are debated, in particular the development and emplacement of the crystalline core, i.e., the Greater Himalayan Crystalline complex (GHC) (Figure 1). Key features of this unit include an inverted metamorphic field gradient extending through the base to its middle or upper structural levels, and two shear zones bounding the GHC from above and below [e.g., *Le Fort*, 1996; *Vannay and Grasemann*, 1998; *Daniel et al*., 2003]. Development of inverted metamorphic field gradients in the Himalaya has been explained by end-member and hybrid models involving postmetamorphic recumbent folding of isograds [*Heim and Gansser*, 1939; *Frank et al*., 1973; *Searle and Rex*, 1989] and/or shearing of isograds [*Jain and Manickavasagam*, 1993; *Hubbard*, 1996; *Vannay and Grasemann*, 2001]; syn-metamorphic shearing of isograds [*Grujic et al*., 1996; *Daniel et al*., 2003], including within the context of a channel flow [*Jamieson et al*., 2004; *Larson et al*., 2010]; emplacement of a crystalline "hot-iron" hanging wall [*Le Fort*, 1975; *Célérier et al*., 2009a, 2009b]; basal accretion of large or small thrust horses [*Reddy et al*., 1993; *Corrie and Kohn*, 2011] commonly in association with surface erosion [*Royden*, 1993; *Herman et al*., 2010]; shear heating [*Molnar and England*, 1990]; and pre-Himalayan heating by Early Paleozoic granite crystallization [*Gehrels et al*., 2003]. Inverted metamorphic field gradients extend below the GHC, and right-way-up metamorphic field gradients persist above it, such that the thermal field is commonly continuous across the bounding shear zones and into the flanking units above and below [e.g., *Bollinger et al*., 2004; *Chambers et al*., 2009].

Additional supporting information may be found in the online version of this article.

[1]Department of Geology and Geophysics, Louisiana State University, Baton Rouge, Louisiana, USA.
[2]Now at Department of Earth and Planetary Sciences, University of Tennessee, Knoxville, Tennessee, USA.
[3]Oil and Natural Gas Corporation of India, Mehsana, Gujarat, India.

Corresponding author: A. Alexander G. Webb, Department of Geology and Geophysics, Louisiana State University, E235 Howe-Russell, Baton Rouge, LA 70803, USA. (awebb@lsu.edu)

©2013. American Geophysical Union. All Rights Reserved.
0278-7407/13/10.1002/tect.20020

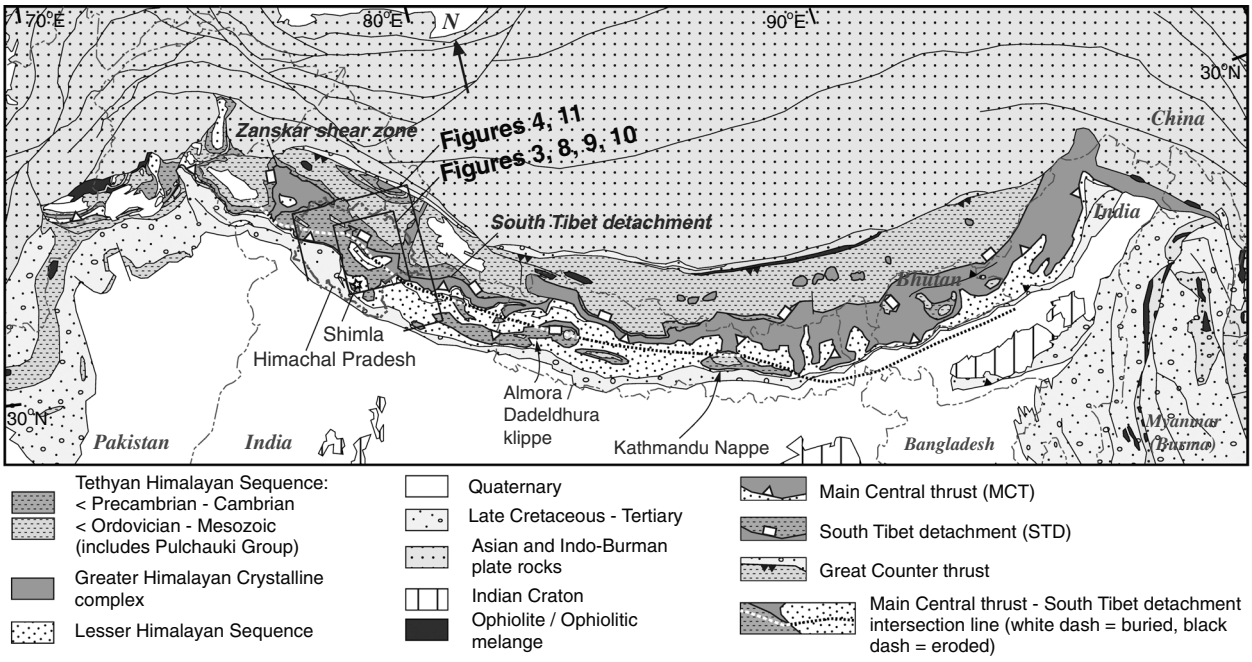

Figure 1. Geological Map of the Himalaya. The dashed line denotes the Indian state of Himachal Pradesh, boxes denotes the boundaries of Figures 3–5 and Figures 9–11. Modified from *Webb et al.* [2011a, 2011b].

[3] The GHC may have been emplaced as a northward-tapering wedge extruded to the south (Figure 2A) [*Burchfiel and Royden*, 1985; *Grujic et al.*, 1996; *Vannay and Grasemann*, 2001]. Alternatively, these rocks may represent a low viscosity channel of middle/lower crustal material driven south by the lateral pressure gradient from the high Tibetan Plateau to the Himalayan foreland [*Nelson et al.*, 1996; *Beaumont et al.*, 2001, 2004; *Hodges et al.*, 2001; *Godin et al.*, 2006]. In both models (referred to as wedge extrusion and channel flow-focused denudation, respectively), the GHC was extruded to the surface during motion along the bounding faults (Figures 2A and B). In contrast, the tectonic wedging model posits that the GHC was emplaced at depth as a southward-tapering wedge (Figure 2C) [*Yin*, 2006; *Webb et al.*, 2007, 2011a, 2011b].

[4] The GHC emplacement models make testable predictions for the distribution of structures and metamorphism in the orogen [e.g., *Jamieson et al.*, 2004; *Webb et al.*, 2011b]. Wedge extrusion and channel flow-focused denudation models predict that the GHC was emplaced at the surface in the Early and Middle Miocene. At this time, the GHC would be bounded by the subparallel bounding shear zones, giving these high grade rocks the appearance of a "pipe to the surface" in cross-sectional view (Figure 2). In map view, these models predict that the bounding faults and GHC consistently separate relatively low grade rocks to north and south. The tectonic wedging model predicts that the bounding faults merge to the south, defining the leading edge of the GHC. South of this fault merger (branch line), the GHC would be missing, and the two low grade units would be in direct thrust contact.

[5] In this study, we test the GHC emplacement models by quantifying regional variations in metamorphic grade across the Himachal Himalaya of northwest India. Previous studies of this region indicate significant along-strike variations

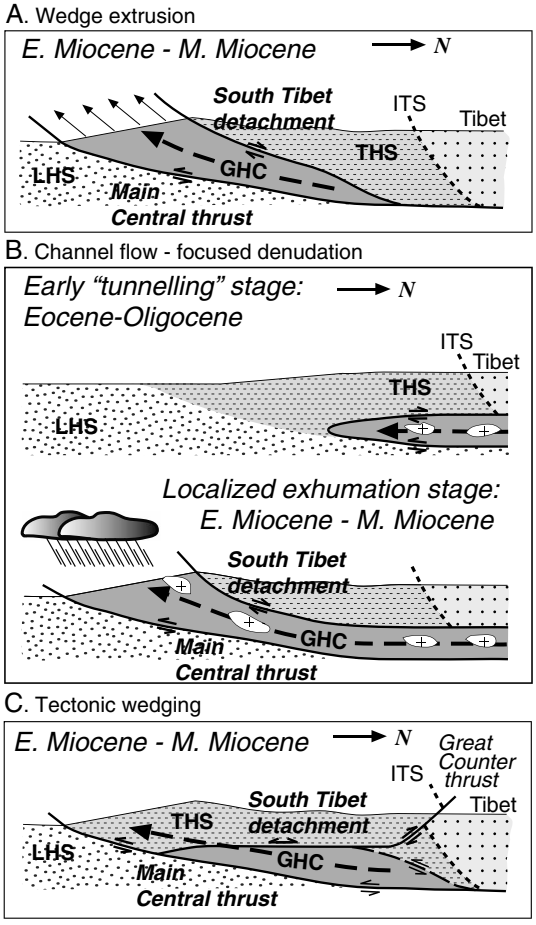

Figure 2. Models for the emplacement of the Greater Himalayan Crystalline Complex (GHC), modified from *Webb et al.* [2011b].

in structural geometry and metamorphic field gradient [*Frank et al*., 1973, 1995; *Bhargava et al*., 1991; *Epard et al*., 1995; *Fuchs and Linner*, 1995; *Thakur*, 1998; *DiPietro and Pogue*, 2004; *Vannay et al*., 2004; *Richards et al*., 2005; *Yin*, 2006; *Webb et al*., 2007, 2011b]. We present petrographic observations, new geothermobarometric determinations obtained via exchange (garnet-biotite) and net-transfer (garnet-biotite-muscovite-plagioclase) reactions [e.g., *Thompson*, 1976; *Ghent and Stout*, 1981], and Ti-in-biotite thermometry [*Henry et al*., 2005].

2. Regional Geology

2.1. The Himalayan Orogen

[6] Himalayan geology is commonly described as a three-layer stack with the crystalline core, the GHC, as the middle layer bounded by faults above and below [e.g., *Hodges*, 2000]. The base of the stack is the Lesser Himalayan Sequence, the Tethyan Himalayan Sequence is the upper layer, and the Main Central thrust (MCT) and South Tibet detachment (STD) are the lower and upper faults, respectively (Figure 1). The MCT emplaced the GHC southwards over the Lesser Himalayan Sequence; the STD displays records of top-north and top-south shear [e.g., *Patel et al*., 1993; *Hodges et al*., 1996]. Metamorphism of the GHC is famously inverted and high grade, ranging from staurolite-zone metapelitic rocks at the base to sillimanite-zone metapelitic rocks and migmatites at the top of the sequence [*Le Fort*, 1975; *Vannay and Grasemann*, 1998]. The Lesser Himalayan Sequence and Tethyan Himalayan Sequence are largely greenschist and subgreenschist facies, but at their respective upper and lower contacts, i.e., adjacent to the GHC, they record temperatures and pressures comparable to GHC conditions [e.g., *Bollinger et al*., 2004; *Crouzet et al*., 2007; *Jessup et al*., 2008; *Célérier et al*., 2009a; *Chambers et al*., 2009; *Cottle et al*., 2011; *Langille et al*., 2012]. Recent work has argued that the GHC is bound to the south by the intersection of the STD with the MCT all along the orogen, such that to the south of this intersection, the MCT places Tethyan Himalayan Sequence rocks directly atop Lesser Himalayan Sequence rocks (Figure 1) [*Webb et al*., 2007, 2011a, 2011b, 2013; *Yin et al*., 2010].

2.2. The Himachal Himalaya

2.2.1. Structural Geometry

[7] The geometry of the MCT is generally well established in the Himachal Himalaya. It is a ~1–2 km thick, top-southwest shear zone which is folded and crops out along an irregular, continuous trace from east to west, at the base of klippen, and along a tectonic window, the Kullu window [Figure 3; e.g., *Vannay et al*., 2004]. However, the trajectory of the STD and the tectonic affinity of the southern MCT hanging wall are controversial [e.g., *Bhargava et al*., 1991; *Fuchs and Linner*, 1995; *Thakur*, 1998; *Grasemann et al*., 1999; *DiPietro and Pogue*, 2004; *Vannay et al*., 2004; *Richards et al*., 2005; *Yin*, 2006; *Webb et al*., 2007, 2011b]. The STD here is a ~300–600 m shear zone featuring top-southwest and top-northeast shear-sense indicators. It has been proposed to (1) extend as a north-dipping structure west from the Himachal region to the Zanskar region, linking to the Zanskar Shear Zone [e.g., *Searle et al*., 1988; *Hodges*, 2000]; (2) terminate in the Himachal region [e.g., *Wyss et al*., 1999; *Vannay et al*., 2004]; or (3) be folded with a top-southwest anticline (the Phojal anticline) and merge with the MCT along the northern margin of the Kullu window [*Thakur*, 1998; *Yin*, 2006; *Webb et al*., 2007, 2011b].

[8] Rocks of the MCT hanging wall to the southwest of the Kullu window are commonly interpreted as (1) divided into GHC rocks and Tethyan Himalayan Sequence rocks [e.g., *DiPietro and Pogue*, 2004], (2) grouped as all GHC rocks [e.g., *Frank et al*., 1973; *Vannay et al*., 2004], or (3) grouped as all Tethyan Himalayan Sequence rocks [*Webb et al*., 2007, 2011b].

[9] The different STD and MCT hanging wall concepts are related and have direct implications for Himalayan tectonic models. For example, if the STD and MCT merge along the northern margin of the Kullu window, then these structures bound the frontal tip of the GHC there and the MCT hanging wall farther southwest consists of Tethyan Himalayan Sequence rocks. The corresponding juxtaposition of Tethyan Himalayan Sequence rocks directly above Lesser Himalayan Sequence rocks across the southern MCT meets predictions of the tectonic wedging model, but not the predictions of wedge extrusion and channel flow-focused denudation models (Figure 2).

[10] Mapping of lithological variations is insufficient to test these concepts because the lower ~5 km of the Tethyan Himalayan Sequence (the Haimanta Group) and the GHC both consist of Late Proterozoic metapelitic and metapsammitic rocks and Early Paleozoic granitic rocks [e.g., *Frank et al*., 1995; *Richards et al*., 2005; *Chambers et al*., 2009; *Webb et al*., 2011b]. However, a review of regional metamorphic constraints indicates that mapping of metamorphic field gradients allows model testing.

2.2.2. Metamorphic Field Gradients: Current Knowledge

[11] The GHC and the Lesser Himalayan Sequence Munsiari Group display an inverted thermal profile, the Tethyan Himalayan Sequence features right-way-up metamorphism, and the controversial portion of the MCT hanging wall to the southwest of the Kullu window has records of both inverted and right-way-up metamorphic field gradients.

[12] Thermobarometric data are largely concentrated along the Sutlej River from the Kullu window to ~50 km farther northeast, and along the northern Beas River (northwest of the Kullu window) [e.g., *Vannay and Grasemann*, 1998; *Jain et al*., 1999; *Vannay et al*., 1999; *Chambers et al*., 2009]. Although the Lesser Himalayan Sequence is largely low grade, along the Sutlej River section, both the Munsiari Group of the Lesser Himalayan Sequence and the GHC record inverted metamorphic field gradients at amphibolite facies conditions [*Vannay and Grasemann*, 1998; *Vannay et al*., 1999; *Caddick et al*., 2007]. From the western limit of the Munsiari Group to its center, temperatures increase from 610°C to 700°C and pressures decrease from 9.0 kbar to 7.0 kbar. Farther northeast along the Sutlej River section, temperature increases from 570°C just above the MCT to 750°C just below the STD, and pressure is constant at 8 kbars. In the Tethyan Himalayan Sequence just above the STD, peak metamorphic conditions drop to T ~ 650°C and P ~ 7.5 kbar [*Vannay and Grasemann*, 1998; *Vannay et al*., 1999; *Chambers et al*., 2009]. Similar results were obtained for the northern Beas River section: metamorphic conditions across

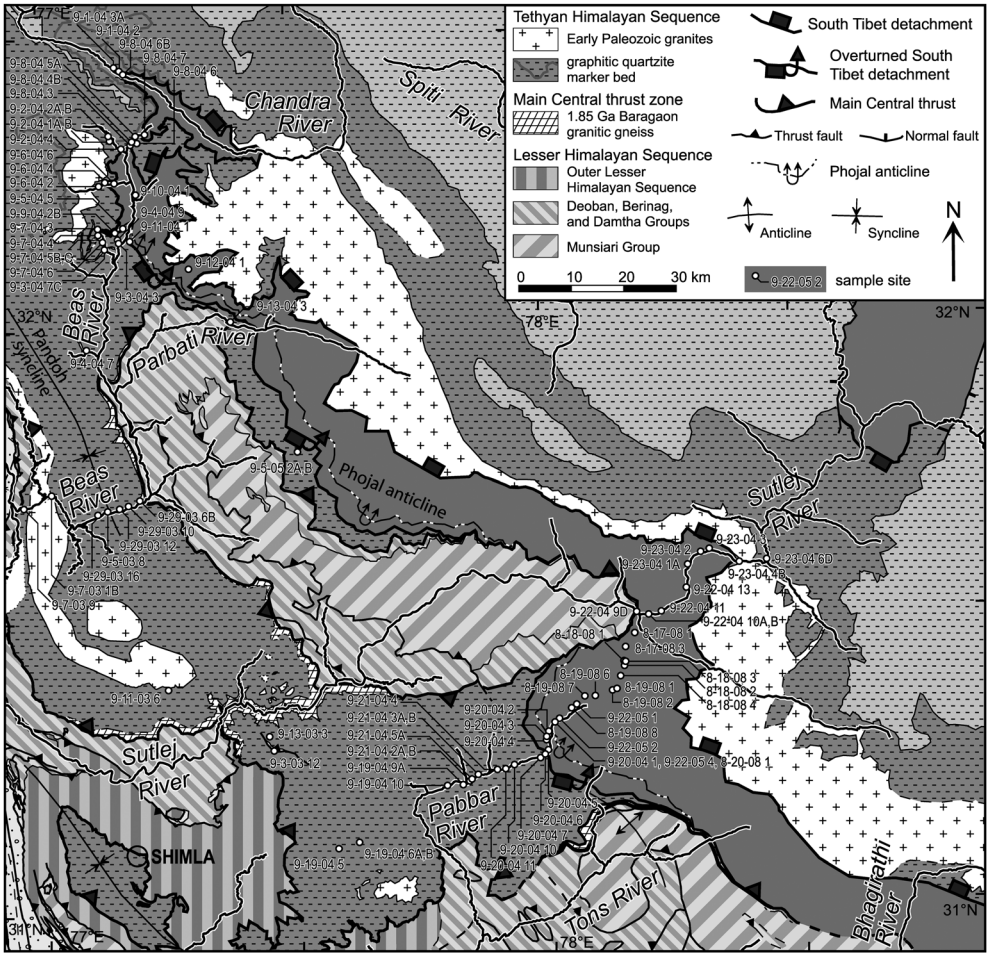

Figure 3. Regional Map of the Himachal Himalaya, based upon our mapping and regional map integration from many sources, as documented in *Webb et al.* [2011b]. Ornaments for map units absent from Figure 1 are shown in the key; other ornaments are as in Figure 1.

the mapped GHC match the highest conditions along the Sutlej River section, and conditions of ~450–650°C and 5–8 kbar are estimated for the adjacent basal Tethyan Himalayan Sequence [*Frank et al.*, 1973; 1995; *Epard et al.*, 1995; *Jain et al.*, 1999; *Walker et al.*, 1999; *Wyss*, 2000; *Verma et al.*, 2005]. In the northeastern Himachal Himalaya, grade progressively decreases upsection across the Tethyan Himalayan Sequence, such that ~5 km above the STD temperatures are at ~250°C [*Wiesmayr and Grasemann*, 2002]. Sparse study across the MCT hanging wall to the southwest of the Kullu window variably suggests that inverted and right-way-up metamorphism may both occur here: quartz recrystallization textures show that the thermal gradient is inverted within the <1.5 km thickness of the MCT shear zone exposed along the Sutlej River [from 535 to 615°C—*Grasemann et al.*, 1999; *Law et al.*, 2011], whereas limited metamorphic mapping and thermobarometry along the Beas River suggest a right-way-up pattern across ~4.5 km of structural thickness above the MCT shear zone [from ~550–600°C to 450–480°—*Epard et al.*, 1995; *Frank et al.*, 1995; *Webb et al.*, 2011b].

[13] Discrimination of the GHC, Munsiari Group, and Tethyan Himalayan Sequence on the basis of metamorphic patterns requires thick sections, because the basal ~1–2 km of all three units experienced roughly similar temperatures and pressures of ~550–650°C and ~7–8 kbar.

2.2.3. Metamorphic Field Gradients: Model Predictions

[14] Four predictive map patterns for the geometry of the STD and the metamorphic variations across the MCT hanging wall in the Himachal region can be generated by combining regional constraints with the three models for GHC emplacement (Figure 4). The first prediction map accommodates the wedge extrusion and channel flow-focused denudation models by showing the STD as a nearly planar northeast-dipping normal fault, which cuts across the entirety of the Himalaya [e.g., *Searle et al.*, 1988; *Hodges*, 2000]; we term this the pipe-planar roof prediction map. The second map also accommodates these models by showing a continuous STD extending to the northwest, but it incorporates field mapping [from *Webb et al.*, 2007] showing the STD as locally folded with the top-southwest overturned Phojal anticline; we term this the pipe-folded roof prediction map. These first and second predictive maps represent approximate end-member pipe-to-the-surface models for a thick versus thin "pipe," respectively. The third map shows the STD folded with the Phojal anticline and merging with the

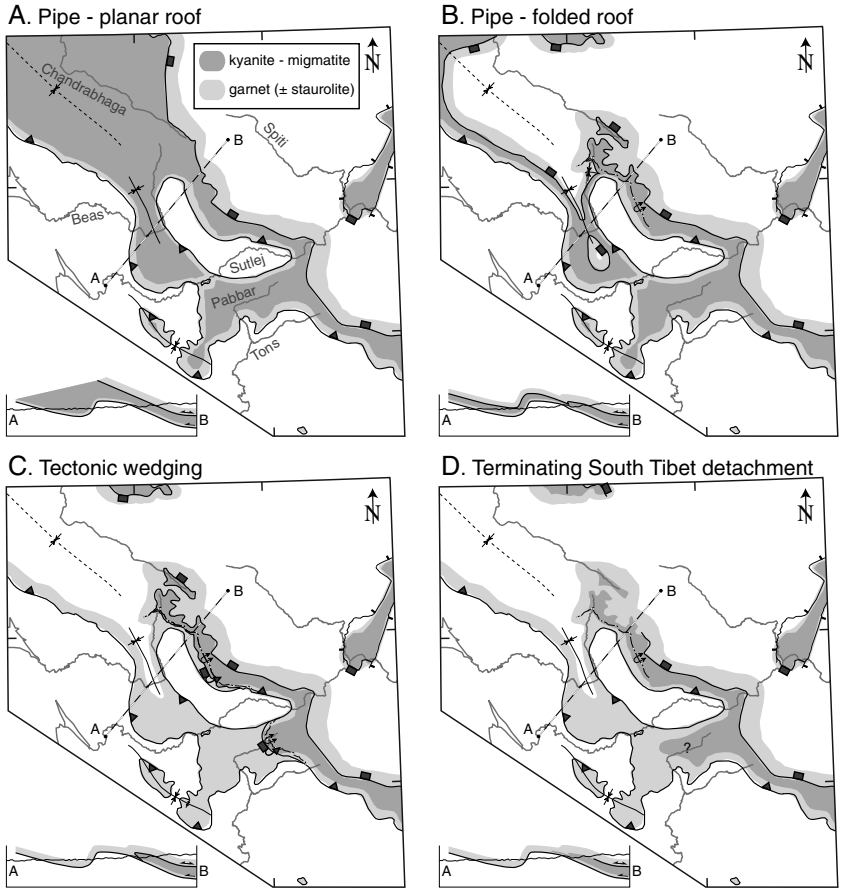

Figure 4. Predictive maps and cross sections, showing major faults and metamorphic distribution, associated with different tectonic scenarios for the Himachal Himalaya, as discussed in the text.

MCT in the overturned limb [*Thakur*, 1998; *Yin*, 2006; *Webb et al*., 2007, 2011b]. This pattern accommodates the tectonic wedging model, so this map is termed the tectonic wedging prediction map. The fourth map incorporates the mapping of *Wyss et al*. [1999] and *Vannay et al*. [2004] by showing the STD slip diminishing to zero in the region; we term this the terminating STD prediction map. The orogen-scale kinematics implied by a termination of STD slip here could be reconciled with the wedge extrusion and channel flow—focused denudation models if STD slip is normal sense and modest ($<$ ~30 km) across the entire system [e.g., *Kohn*, 2008; *Long and McQuarrie*, 2010]. For such a model, it is not immediately obvious how to distinguish the GHC from the Tethyan Himalayan Sequence to the southwest of the STD termination line. In subsequent discussion of this model, we generally follow *Long and McQuarrie's* [2010] suggestion to use metamorphic grade, classifying all coherent rock packages of the MCT hanging wall with garnet grade rocks at the base and a right-way-up metamorphic field gradient as Tethyan, and packages with garnet grade rocks at the base and an inverted metamorphic field gradient extending at least up to kyanite grade as GHC.

[15] Differences in metamorphic field gradients and positions of structures in the four prediction maps can be used to test the validity of the associated tectonic models. Regional structural geology is presented in a complementary publication [*Webb et al*., 2011b]. Here, we document metamorphic field gradients across three target areas. The first target area is to the northwest of the Kullu window along the Beas River, referred to as the northern Beas transect. Here, the pipe-planar roof map predicts the region to be dominated by high grade rocks of the GHC, whereas the other three maps predict outcropping of both GHC and the lower grade Tethyan Himalayan Sequence. The second target is a northeast-southwest transect to the southeast of the Kullu window that largely follows the Pabbar River and is referred to as the Pabbar transect. Both "pipe" prediction maps show high grade rocks along this transect, the tectonic wedging map shows a decrease in grade to the southwest associated with the postulated overturned STD, and the terminating STD model could have a similar decrease. The third target area is the MCT hanging wall section along the Beas River to the southwest of the Kullu window, referred to as the southern Beas transect. This transect has the greatest preserved structural thickness of the MCT hanging wall to the southwest of the Kullu window, ~4.5 km. This structural thickness allows us to complement early work [*Epard et al*., 1995; *Frank et al*., 1995; *Webb et al*., 2011b] in order to determine whether the MCT hanging wall here preserves an inverted metamorphic gradient or a right-way-up gradient,

a key predictive distinction between pipe-to-the-surface models and the other models.

3. Methods

[16] Sixty samples were chosen for detailed petrologic descriptions using hand samples and polished thin sections cut perpendicular to the foliation and parallel to the lineation. An Olympus SZX16 reflective light microscope and a Leica DM EP petrographic microscope were used to view and document thin sections. Possible ranges of peak metamorphic conditions for metapelites are determined by reference to the petrogenetic grid taken from *Vannay and Grasemann* [1998] for similar rock types collected along the Sutlej Valley (Figure 5). Mineral abbreviations follow *Kretz* [1983] and *Bucher and Frey* [1994].

[17] Electron microprobes at the University of California, Los Angeles (UCLA) and Louisiana State University, Baton Rouge (LSU) were used to acquire mineral chemical data for (1) exchange (garnet-biotite) and net-transfer (garnet-biotite-muscovite-plagioclase) thermobarometry and (2) Ti-in-biotite thermometry [*Henry et al*., 2005]. The majority of the samples were analyzed at UCLA using the JEOL JXA-8200 electron microprobe, with four samples analyzed using the JEOL JXA733 Superprobe at LSU. The operating conditions were set to 15 kV accelerating voltage, with sample current of 15 nA at UCLA versus 10 nA at LSU for all phases. For standardizing, natural minerals were used. All phases used a beam focused at <1 μm diameter except for the micas which had spot sizes between 3 and 7 μm. Microprobe analysis was performed on garnet grains along with nearby, but not directly adjacent, biotite, muscovite, and plagioclase grains.

[18] The programs THERMOCALC [v.3.33, *Holland and Powell*, 1998] and TWQ [*Berman*, 2007] were used in determining exchange (garnet-biotite) and net-transfer (garnet-biotite-muscovite-plagioclase) intersections for pelitic rocks. For THERMOCALC determinations, activity coefficients for each mineral phase were calculated using the AX software, P-T estimates were calculated using the updated *Holland and Powell* [1998] data set (tc-ds55.txt), and the average P-T mode was used to make the P-T estimates. For TWQ determinations that do not yield a pressure result, temperature was calculated assuming pressure of 8 kbar. Garnet X-ray maps and zoning profiles were done on several representative samples to check for zoning patterns. X-ray maps with 2 μm pixels with a dwell time of 60 ms per pixel were collected with an accelerating voltage of 15 kV and a current of 100 nA. Several garnets showed slight reversal in zoning pattern at the rims related to retrograde resorption. For reabsorbed garnet grains, data at the lowest Mn value of each garnet (just before the reversal in zoning pattern at the rims) was used in order to estimate peak metamorphic conditions for both TWQ and THERMOCALC programs.

[19] Two techniques were employed to provide a dense assessment of regional temperature variations: Ti-in-biotite thermometry and analysis of quartz recrystallization microstructures. Ti-in-biotite temperatures were calculated following the procedure described in *Henry et al*. [2005] (Table 3). The Ti-in-Biotite thermometer was developed for metapelites that contain Qtz, Bt, Gr, a Ti-saturating phase (Spn, Rt, Ilm), and an aluminous phase (St, Ky, Sil, Crd, Chl, and, Cld). *Henry et al*. [2005] determined the precision of this thermometer to be 24°C at lower temperatures (<600°C), improving to 12°C at high temperature (>700°C). Modes of dynamic quartz recrystallization vary as a function of strain rate and temperature, such that at common strain rates bulging recrystallization

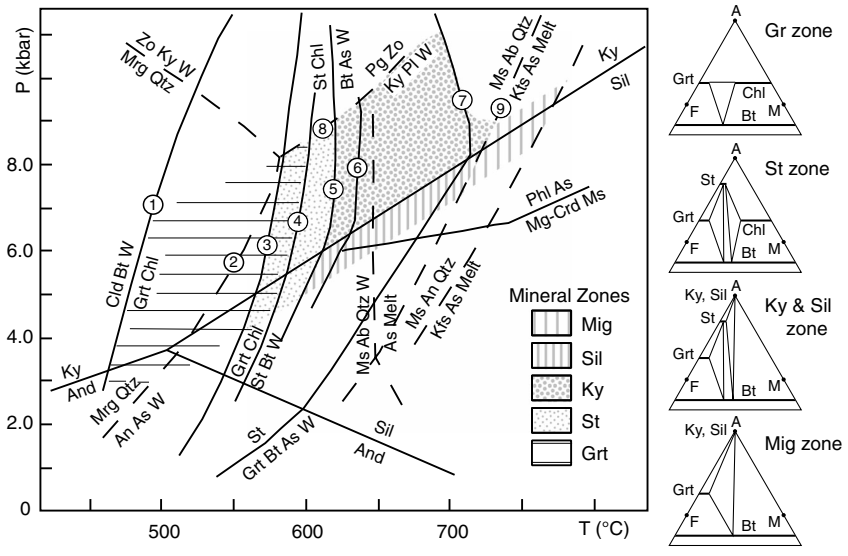

Figure 5. Petrogenetic grid for pelites adopted from *Vannay and Grasemann* [1998]. Solid lines correspond to reactions in the (Mn)KFMASH system and dashed lines correspond to reactions in the CKNASH system. Numbers indicate limiting reactions referred to in the text. Reaction 3 is the KFMASH equivalent of reaction 4. Reaction 6 is Mg-Chl + Ms = Phl + As + W (the water [W] is released on the high temperature side). Shaded regions show Barrovian metamorphic zones, and the mineralogy of these zones is summarized in the accompanying AFM diagrams.

generally occurs at temperatures of ~250–400°C, subgrain rotation occurs at higher temperatures up to 500–550°C, and above that threshold grain boundary migration dominates [*Hirth and Tullis*, 1992; *Stipp et al*., 2002]. Experimental results demonstrate that at elevated strain rates, as may be recorded across much of the Himalayan orogen, temperatures associated with each recrystallization mechanism may be higher [*Hirth and Tullis*, 1992]. Recrystallization modes were determined by thin section inspection using the petrographic microscope [cf. *Célérier et al*., 2009a; *Long and McQuarrie*, 2010].

4. Petrology

[20] Metasedimentary rocks of the MCT hanging wall in the Himachal Himalaya are dominated by metapsammites and metapelites, with minor paragneisses and calc-silicate rocks. Below, description of lithologies is organized by our three target areas.

4.1. Northern Beas Transect

[21] The rock types sampled from the GHC and Tethyan Himalayan Sequence of the northern Beas valley section were primarily metapelites and metapsammites. The main metasedimentary rock type in the region for both the GHC and Tethyan Himalayan Sequence is metapsammite, with subordinate metapelitic and calc-silicate rocks in the Tethyan Himalayan Sequence and metapelites and migmatite in the GHC. Metapsammites and metapelites commonly contain Grt + Bt + Pl + Qtz ± Chl ± Ms ± St ± Ky with accessory minerals variably including Zrn, Ap, Rt, Ttn, Cal, Ilm, Gr, and Ep (Table 1). The highest temperature rocks for the region are observed in the GHC adjacent the STD.

[22] GHC metapelitic sample AW 9-10-04 (1) contains the major mineral assemblage Grt + Bt + Pl + Qtz + Ms + Ky consistent with kyanite grade metamorphism (Figure 5 and Table 1). This assemblage is restricted to T ≈ 610–720°C and P ≈ 6–11 kbar by the reactions Ky = Sil, (5), (7), (8), as displayed on the petrogenetic grid (Figure 5). Two GHC migmatite samples (AW 9-1-04 (6B), AW 9-11-04 (1)) contain assemblage Melt + Kfs + Bt + Ms + Qtz + Pl + Grt, representative of migmatite grade rocks (Figure 5 and Table 1). Minimum melting conditions for this assemblage is restricted above reaction (9), so conditions are likely to be T ≈ 700–780°C and P ≈ 7.5–9.5 kbar (Figure 5). Melting in these rocks could have occurred as low as T ≈ 650°C due to vapor-present melting for the assemblage Ms + Pl + Qtz [*Spear*, 2003].

[23] Two metapelites samples from moderate to high structural positions (AW9-6-04 (4), AW 9-8-04 (5A)) contain staurolite along with Grt + Qt + Pl + Bt + Ms + Chl. This mineral assemblage is constrained on the petrogenetic grid for pelite rocks to T ≈ 560–620°C through reactions (3) and (5) (Figure 5). Associated calc-silicate rocks are metamorphosed under epidote-amphibolite facies conditions and contain the prograde major mineral assemblage Qtz + Grt + Bt + Am + Pl ± Ep.

4.2. Pabbar Transect

[24] Samples along the Pabbar transect were collected perpendicular to the regional orogenic strike, from sample AW 8-17-08 (1) in the northeast to sample AW 9-19-04 (5) in the southwest (Figure 3). Distinctions in metamorphic grade recorded by mineral assemblages are restricted to the middle and southwestern samples. In the middle of the transect, sillimanite- and migmatite-bearing rocks represent the highest petrographically constrained temperatures at ~700°C. In the southwest, Barrovian-type garnet grade rocks record the lowest temperatures at < ~610°C. Metapelites and metapsammites make up the majority of rock types in this region, with minor migmatite, paragneiss, and calc-silicate. Accordingly, the mineral assemblage Qtz + Grt + Bt + Pl ± Ms Chl dominates the area. Common accessory minerals for all rock types include Zrn, Ap, Rt, Ttn, Cal, Ilm, Gr, and Ep. Some samples show extensive retrogression of garnet and amphibole to chlorite.

[25] The mineral assemblages of the seven northernmost samples (metapsammites featuring the prograde mineral assemblage Qtz + Grt + Bt + Pl ± Ms are poorly constrained on the petrogenetic grid limiting P-T estimates (Figure 5). South of these samples, P-T conditions can be estimated for sample AW 9-20-04 (1) which displays migmatitic textures and contains the assemblage Melt + Kfs + Bt + Ms + Qtz + Pl + Grt. This assemblage indicates minimum temperatures of 700°C (as above). Immediately southwest, sample AW 9-20-04 (2) marks the first appearance of a calc-silicate, with the prograde mineral assemblage Qtz + Grt + Bt + Am + Pl + Ep. Farther southwest, sample AW 9-20-04 (3) contains Sil + Grt + Qt + Pl + Bt + Ms (Figure 6A). Sillimanite in this sample occurs as small fibrolite bundles. Reactions (6) and (11) constrain this assemblage on the petrogenetic grid to T ≈ 610–720°C and P ≈ 6–8.5 kbar (Figure 5). Farther southwest, sample AW 9-20-04 (4) contains the major mineral assemblage Melt + Kfs + Sil + Bt + Qtz + Pl, again indicating minimum temperatures of 700°C (Figure 6B). This sample marks the farthest southwest occurrence of aluminosilicate identified along the transect. Samples farther southwest along the Pabbar Valley transect are dominated by metapsammites with the prograde mineral assemblage Qtz + Grt + Bt + Pl ± Ms. Interspersed within the metapsammites, <25 cm thick calc-silicate lenses occur containing the typical prograde mineral assemblage Qtz + Grt + Bt + Am + Pl ± Ep. This assemblage is broadly suggestive of epidote amphibolite facies. A systematic reduction in grain size from an average of 0.45 mm to 0.20 mm is observed southwestward through these metapsammite and calc-silicate samples, suggesting decreasing P-T conditions. Sample AW 9-19-04 (5), the southernmost sample studied along the transect, contained the prograde mineral assemblage Grt + Bt + Chl + Ms + Qtz (Figure 6C). This mineral assemblage in the MnKFMASH system is constrained to T ≈ 460–610°C by reactions (1) and (4) (Figure 5).

4.3. Southern Beas Transect

[26] Rocks here are folded with the Pandoh syncline, such that the MCT outcrops to the northeast and the southwest. We examined samples AW 9-29-03 (10), AW 9-29-03 (12), AW 9-5-03 (8), AW 9-29-03 (16), and AW 9-29-03 (7), which extend from the Kullu Window MCT to the main MCT trace exposed to the southwest. The first two and last two samples are metapelites containing the prograde assemblage Qtz + Bt + Chl + Ms + Pl + Grt. Temperature constraint for this mineral assemblage in the MnKFMASH system is constrained to T ≈ 460–610°C by reactions (1) and (4) (Figure 5). AW 9-5-03 (8), which represents the core of

Table 1. Sample Mineralogy[a]

:Qtz + Bt + Pl	Chl	Ms	Grt	Ep	Amp	St	Ky	Sil	Kfs	Rt/Ttn/Ilm	Gr	Tur	Zrn	Cal	Ap
Pabbar Transect															
AW 9-19-04 (5)	X	X	X	-	-	-	-	-	-	X	-	-	-	-	-
AW 9-19-04 (6B)	-	X	X	X	-	-	-	-	-	-	-	-	-	-	-
AW 9-19-04 (9A)	R	X	X	-	-	-	-	-	-	X	X	-	-	-	-
AW 9-19-04 (10)	X	X	X	-	-	-	-	-	-	X	-	-	-	-	-
AW 9-20-04 (1)	-	X	-	-	-	-	-	-	X	X	-	X	-	-	X
AW 9-20-04 (2)	-	-	X	X	X	-	-	-	-	X	-	-	-	-	-
AW 9-20-04 (3)	-	X	X	-	-	-	-	X	-	X	X	X	X	-	-
AW 9-20-04 (4)	-	-	X	-	-	-	-	X	X	X	-	-		-	X
AW 9-20-04 (5)	-	X	-	X	-	-	-	-	-	X	-	-	X	-	X
AW 9-20-04 (6)	-	X	-	X	-	-	-	-	-	-	-	X	-	-	-
AW 9-20-04 (7)	-	X	X	X	-	-	-	-	-	X	-		-	-	-
AW 9-20-04 (10)	R	X	X	X	-	-	-	-	-	X	-	X	X	X	-
AW 9-20-04 (11)	R	X	X	X	-	-	-	-	X	X	-	X	-	-	X
AW 9-21-04 (2A)	R	X	X	-	X	-	-	-	-	X	-	X	-	-	-
AW 9-21-04 (2B)	-	X	X	-	-	-	-	-	-	X	-	X	X	-	-
AW 9-21-04 (3A)	R	-	X	X	X	-	-	-	-	X	-	-	X	-	X
AW 9-21-04 (3B)	-	-	X	X	X	-	-	-	-	X	-	-	-	-	-
AW 9-21-04 (4)	R	-	X	X	-	-	-	-	-	X	-	-	X	-	X
AW 9-21-04 (5A)	-	X	X	-	-	-	-	-	-	X	X	X		X	-
AW 9-22-05 (1)	-	X	X	X	-	-	-	-	-	X	X	X	X		X
AW 9-22-05 (2)	R	-	X	X	-	-	-	-	X	-	-			X	-
AW 9-22-05 (4)	R	X	X	X	-	-	-	-	-	-	-	X	X	-	-
AW 8-17-08 (1)	X	X	X	-	-	-	-	-	-	X			X	-	X
AW 8-17-08 (3)	X	X	X	X	-	-	-	-	-	-	X	X	X	-	-
AW 8-18-08 (1)	-	X	X	-	-	-	-	-	-	-	-	-	-	-	-
AW 8-18-08 (2)	R	X	X	X	-	-	-	-	-	X	-	-	-	-	-
AW 8-18-08 (3)	R	X	X	-	-	-	-	-	-	X	X	-	-	-	X
AW 8-18-08 (4)	R	X	X	-	-	-	-	-	-	-	-	-	X	-	X
AW 8-19-08 (1)	R	X	X	-	-	-	-	-	X	X	X	-	-	-	-
AW 8-19-08 (2)	-	X	X	-	-	-	-	-	-	-	-	-	X	-	-
AW 8-19-08 (6)	-	X	X	-	-	-	-	-	X	-	-	-	X	-	-
AW 8-19-08 (7)	R	-	X	-	-	-	-	-	-	X	X	-	X	-	-
AW 8-19-08 (8)	R	X	X	X	-	-	-	-	-	X	X	-	-	-	-
AW 8-20-08 (1)	R	X	X	X	-	-	-	-	-	X	-	X	X	X	X
AW 9-3-03 (12)	-	X	X	X	-	-	-	-	-	X	X	-	-	-	-
AW 9-11-03 (6)	-	-	X	-	-	-	-	-	-	X	-	-	-	-	-
AW 9-13-03 (3)	-	-	X	-	-	-	-	-	-	X	-	-	-	-	-
Southern Beas															
AW 9-5-03 (8)	X	X	-	-	-	-	-	-	-	X	X	-	-	-	-
AW 9-7-03 (9)	X	X	X	-	-	-	-	-	-	X	X	-	-	-	-
AW 9-29-03 (9)	X	X	X	-	-	-	-	-	-	X	X	-	-	-	-
AW 9-29-03 (10)	X	X	X	-	-	-	-	-	-	X	-	-	-	-	-
AW 9-29-03 (12)	X	X	X	-	-	-	-	-	-	X	-	X	-	-	-
AW 9-29-03 (16)	X	X	-	-	-	-	-	-	-	X	-	-	-	-	-
Northern Beas															
AW 9-1-04 (2)	-	X	X	-	-	-	-	-	-	X	-	-	X	-	X
AW 9-1-04 (3A)	X	X	X	X	-	-	-	-	-	X	-	X	-	-	X
AW 9-1-04 (6B)	-	X	X	X	-	-	-	-	X	X	X	-	-	-	X
AW 9-2-04 (1A)	X	-	-	X	X	-	-	-	-	X	-	-	-	-	-
AW 9-2-04 (2B)	-	X	-	-	-	-	-	-	-	X	X	X	-	-	-
AW 9-2-04 (4)	X	X	X	-	-	-	-	-	-	X	-	-	X	-	X
AW 9-6-04 (2)	X	X	X	-	-	-	-	-	-	X	X	X	-	-	X
AW 9-6-04 (4)	X	X	X	-	-	X	-	-	-	X	X	X	X	-	-
AW 9-7-04 (3)	-	-	X	-	-	-	-	-	-	X	-	-	X	-	X
AW 9-8-04 (3)	X	X	X	-	-	-	-	-	-	X	-	-	X	-	X
AW 9-8-04 (4B)	X	X	X	-	-	-	-	-	-	X	X	X	-	-	-
AW 9-8-04 (5A)	X	-	X	-	-	X	-	-	-	X	X	-	X	-	X
AW 9-8-04 (6)	-	-	X	X	X	-	-	-	-	X	-	-	-	-	-
AW 9-8-04 (7)	-	X	X			-	-	-	-	X	X	X	X	-	X
AW 9-9-04 (2B)	-	-	X	X	X	-	-	-	-	X	-	-	-	-	-
AW 9-10-04 (1)	-	X	X	-	-	-	X	-	-	X	-	X	-	-	-
AW 9-11-04 (1)	-	X	X	-	-	-	-	-	X	X	X	X	X	-	-

[a]Mineral abbreviations after *Kretz* [1983] and *Bucher and Frey* [1994]. X indicated the presence of the mineral. – indicates the absence of the mineral. R, mineral present only as a retrograded breakdown product.

the Pandoh syncline and is the structurally highest rock, also contains prograde Qtz + Bt + Chl + Ms + Pl but lacks Grt. This could indicate crossover into the biotite zone, which is restricted to below $T \approx 475°C$ by reaction (1) (Figure 5). Another indication of relatively low temperature is the preservation of detrital quartz grains in this sample and other samples (AW 9-29-03 12, AW 9-29-03 16) in the core of the Pandoh syncline (Figure 6D).

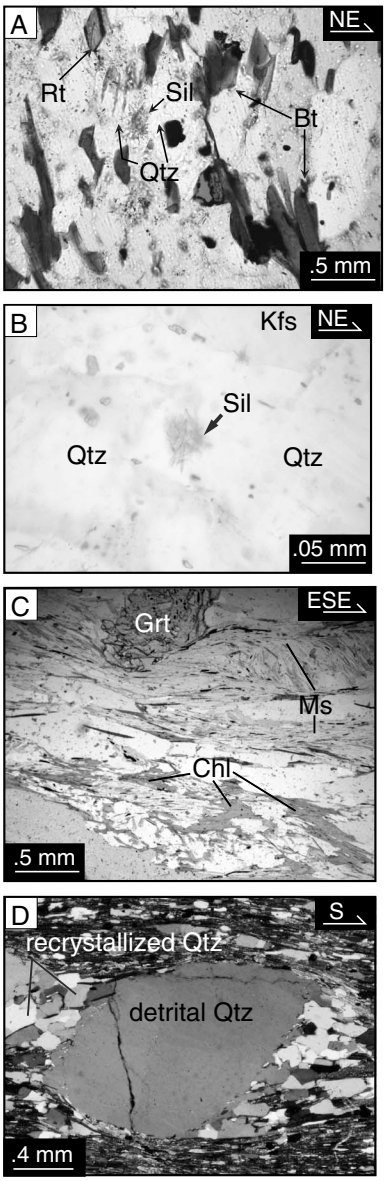

Figure 6. Photomicrographs showing key mineralogy for metamorphic history determinations. (A) Sillimanite fibrolite clusters growing at boundary of quartz in migmatite (AW 9-20-04 (3)). (B) Sillimanite fibrolite clusters growing at boundary of quartz in pelitic gneiss (AW 9-20-04 (4)). (C) Prograde chlorite surrounded by muscovite in pelitic schist (AW 9-19-04 (5)). A deformed garnet can be seen at the top of the picture. (D) Preserved detrital quartz grain in pelitic schist (AW 9-29-03 (12)). This sample comes from the core of the Pandoh syncline, along the southern Beas transect. *Frank et al*. [1995] have correlated rocks here with the Manjir unit of the basal Tethyan Himalayan Sequence (Haimanta Group) because the Manjir unit contains similarly large detrital grains.

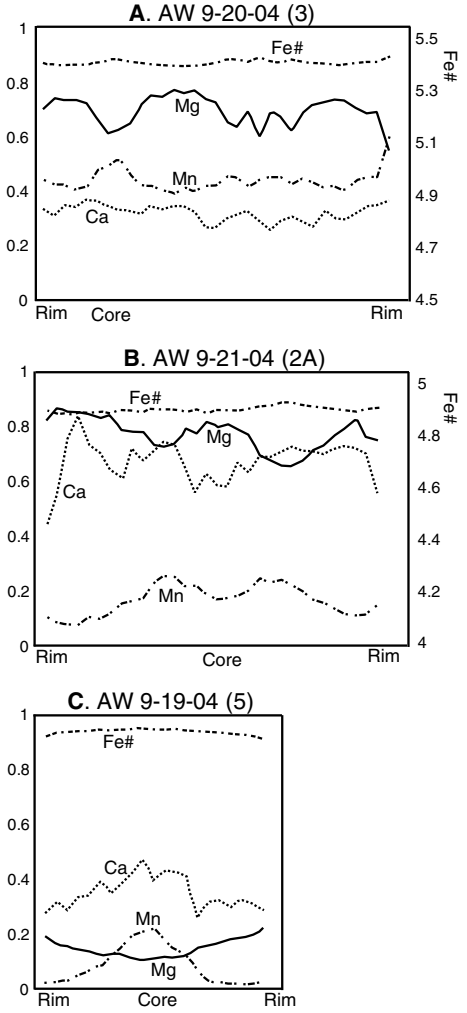

Figure 7. Garnet Zoning Profiles. (A) Garnet with a flat Mn profile, which still retains Ca, Mg, zoning profiles. (B) Garnet profile showing possible prograde growth of two garnet cores (marked by Mn peaks) that nucleated discretely and then grew together. A reversal in zoning profile is seen at the very edge of samples AW 9-21-04 (2A) and AW 9-20-04 (3). (C) Representative metapelite prograde chemical zoning profiles- bell-shaped Mn and rimward decreasing Fe#-shown for sample AW 9-19-04 (5). Decrease in Ca content indicated decrease in pressure during growth (in the absence of other major Ca-bearing phases).

5. Thermobarometry

[27] Fourteen samples from the Pabbar transect and one from the southern Beas transect were analyzed using exchange and net-transfer reaction thermobarometry; 38 samples from the three transects were analyzed using the Ti-in-biotite thermometer.

5.1. Garnet Zoning Patterns

[28] Garnet zoning information was collected for most samples that were analyzed for exchange and net-transfer thermobarometry. Specifically, element maps or profiles were collected for 13 of 15 samples (Figure 7 shows profiles for AW 9-19-04 (5), AW 9-20-04 (3), and AW 9-21-04 (2A); Mn maps for samples AW 9-29-03 (12), AW 9-3-03-(12), AW 9-11-03-(6), AW 9-13-03-(3), and AW 9-21-04-(2B) can be found in *Webb et al*. [2011b]; data for samples AW 9-19-04 (6B), AW 9-19-04 (10), AW 9-20-04 (7), AW 9-20-04 (10), and AW 9-22-05 (2) are contained in Supplementary File 1). Samples AW 9-3-03-(12), AW 9-11-03-(6),

AW 9-13-03-(3), AW 9-19-04 (5), AW 9-19-04 (6B), and AW 9-20-04 (10) have bell-shaped Mn zoning patterns associated with prograde growth (e.g., Figure 7C). Sample AW 9-20-04 (10) has clearly been partially resorbed—the zoning pattern is truncated. Garnet in Sample AW 9-20-04 (3) is the only sample to show almost homogeneous Mn zoning compositions (excepting the very center of the garnet) and yet retains prograde Fe, Mg, and Ca zoning profiles (Figure 7A). Short-wavelength variations in this profile correlate with inclusions, and garnet analyses next to those inclusions show variations consistent with diffusion modification. The garnet zoning pattern of sample AW 9-21-04 (2A) suggests that two garnets may have nucleated separately, but then grown together during prograde metamorphism (Figure 7B). Element maps for samples AW 9-19-04 (10), AW 9-20-04 (7), and AW 9-22-05 (2) suggest that the normal bell-shaped growth zoning of Mn may occur, but the garnets are both too poikilitic and too resorbed to be certain (Supplementary File 1). Garnet in sample AW 9-29-03 (12) is very small (<0.2 mm) and shows no zoning.

5.2. Exchange and Net-Transfer Reaction Thermobarometry

[29] Thermobarometry along the Pabbar transect reveals spatially coherent temperature variations (Figure 8, Tables 2 and 3, and Supplemental File 2). The northern part of the transect yields results of $T \approx 650°C$, with values gradually increasing southward to AW 9-20-04 (3), a sillimanite bearing sample with TWQ results of $T = 683°C$ and $P = 7.2$ kbars. Results for the next five samples to the southwest range show a range in temperatures from $T = 608°C$ to $T = 710°C$ and pressures from $P = 8.3$ kbars to $P = 9.6$ kbars. However, three of these five samples show garnet resorption (AW 9-19-04 (10), AW 9-20-04 (7), and AW 9-20-04 (10), as discussed above) and thus may not represent equilibrium conditions. The remaining two samples both come from the same site (AW 9-21-04 (2A) and AW 9-21-04 (2B)) and yield temperature results at the lower end of the range (608°C and 617°C, respectively). Farther southwest, peak temperature results decrease further. Sample AW 9-19-04 (6B) yields TWQ results of $T = 574°C$ and $P = 8.9$ kbar,

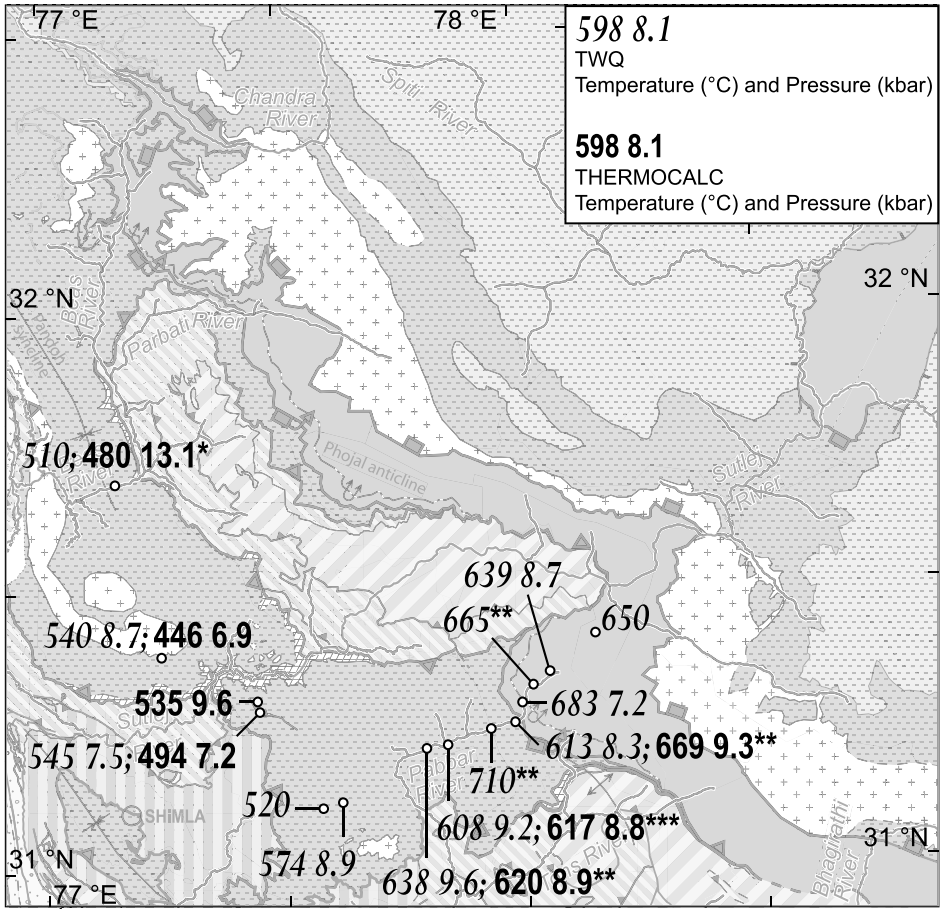

Figure 8. Regional Map (same as Figure 3) showing THERMOCALC and TWQ results. One result is marked with a "*" (i.e., sample AW 9-29-03 12 from the southern Beas transect). As noted in the text, the anomalously high-pressure result for this sample (13.1 kbar) reflects the low An content (An_1) of the feldspar, which is outside the range of the barometer. Results marked with "**" are from samples with garnet textures indicating partial resorption (see text), so the calculated temperatures and pressures are not necessarily reflecting an equilibrium assemblage. We used data at the lowest Mn value of each garnet to estimate peak metamorphic conditions. One set of results is marked with a "***" to denote that the TWQ and THERMOCALC results at this site come from distinct samples, AW 9-21-04 (2A) and AW 9-21-04 (2B).

Table 2. Representative Analyses for Thermobarometry Results

	AW 9-20-04 (3)				AW 9-19-04 (5)			
Oxide	Grt	Bt[a]	Pl	Ms	Grt	Bt[a]	Pl	Ms
SiO_2	38.722	34.845	64.575	44.47	37.24	35.57	64.23	43.86
TiO_2	0.050	2.947	0.000	1.187	0.056	1.4297	0.0944	0.3093
Al_2O_3	18.201	18.675	21.773	32.268	19.84	19.85	21.87	38.09
Cr_2O_3	0.001	0.000	0.000	0.044	0.00	0	0.0215	0.0308
FeO	34.420	19.713	0.000	1.529	36.17	21.21	0.0519	1.253
MnO	0.556	0.104	0.000	0.000	0.23	0.0146	0	0
MgO	3.547	8.808	0.000	1.309	1.76	8.79	1.8256	0.6709
CaO	4.377	0.012	2.635	0.000	3.30	0	0.0972	0
Na_2O	0.013	0.217	10.254	0.810	0.00	0.2422	10.07	1.9537
K_2O	0.000	9.177	0.089	10.011	0.00	8.81	0.0578	8.76
Total	99.887	94.948	99.326	91.362	98.596	95.9165	98.3184	94.9277

Note: mineral abbreviations after [*Kretz*, 1983].
[a]Ti-In-Biotite thermometer uses the TiO_2, FeO, and MgO normalized values.

and results for the most southern sample, AW 9-19-04 (5), show further temperature decrease to T = 520°C. TWQ and THERMOCALC results for samples AW 9-3-03 (12), AW 9-11-03 (6), and AW 9-13-03 (3), which are along strike and within ~20 km of the Sutlej River, give similar results of T < 550°C [*Webb et al*., 2011b].

[30] TWQ and THERMOCALC results were obtained for sample AW 9-29-03 (12) of the southern Beas transect. TWQ yielded T = 510°C; THERMOCALC yielded T = 480°C and P = 13.1 kbar. This pressure is likely an overestimate because the exceptionally low An content (An_1) of the feldspar is below the calibration range of the barometer [*Ghent and Stout*, 1981].

5.3. Ti-in-Biotite Thermometry

[31] Six of the 38 samples investigated using the Ti-in biotite thermometer (Figure 9, Table 3, and Supplemental File 3) contain the calibration mineral assemblage specified by *Henry et al*. [2005] (viz. AW 9-20-04 (3), AW 9-5-03 (8), AW 9-2-04 (4), AW 9-6-04 (4), AW 9-8-04 (4B), and AW 9-8-04 (5A). All analyzed samples contained a Ti phase and quartz. Twenty samples lacked an apparent Al phase. However, the Al_2O_3 content of biotite in these samples was generally above the 17 wt%, which is typical of biotite at or very near Al saturation. Only 14 of the analyzed samples contained graphite. The lack of graphite can produce accurate temperature results, but with large deviations [*Henry et al*., 2005]. We found when at least 12 biotite locations are measured the precision of method is at most ±27°C at one standard deviation.

[32] Results across the northern Beas transect can be divided into three groups: T > 650°C, T < 600°C, and 600°C T < 650°C. The first group consists only of kyanite-bearing GHC sample AW 9-10-04 (4), with the highest determined temperature of 666 ± 6°C. Remaining samples are of the immediate STD hanging wall [following the mapping of *Webb et al*., 2007]. Samples AW 9-8-04 (4B), AW 9-8-04 (5A), AW 9-2-04 (4), and AW 9-6-04 (4) contain the calibration mineral assemblage and yield temperatures between 559°C and 570°C. Samples AW 9-1-04 (2), AW 9-2-04 (2B), AW 9-7-04 (3), and AW 9-8-04 (3) likewise yield temperatures below 600°C; results for samples AW 9-1-04 (3A), AW 9-6-04 (2), and AW 9-8-04 (7) are between 611°C and 636°C.

[33] The northernmost sample analyzed along the Pabbar transect, AW 8-17-08 (1), yields T = 573 ± 10°C. To the southwest, determined temperatures generally increase up to 682 ± 6°C and 678 ± 13°C (samples AW 9-20-04 (3) and AW 9-20-04 (5), respectively). Farther southwest, temperature drops to 638 ± 16°C (sample AW 9-20-04 (7)). The next six samples along the transect yield temperatures alternating from above 675°C to below 655°C, with a high of 684 ± 11°C recorded by sample AW 9-20-04 (10) and a low of 616°C for sample AW 9-20-04 (2B). The two most southern samples yield lower temperatures of 541 ± 18°C and 598 ± 11°C (AW 9-19-04 (5) and AW 9-19-04 (6B), respectively). To the northwest (along strike of the two southern samples), three samples yield temperatures between 563°C and 577°C.

[34] Ti-in-biotite temperatures between 600°C and 573°C were obtained for four samples across the core of the Pandoh sincline exposed along the southern Beas transect.

6. Quartz Recrystallization Textures

[35] Thin sections from 73 samples yield quartz recrystallization mode information. All but one analyzed sample was dominated by subgrain rotation and/or grain boundary migration textures (Figure 10 and Supplemental File 4).

[36] Along the northern Beas transect, three samples display subgrain rotation textures, 11 display grain boundary migration textures, and 11 samples are intermediate, showing both textures. Results correlate with structural position relative to the STD [following the mapping of *Webb et al*., 2007]: e.g., subgrain rotation textures are limited to the hanging wall whereas grain boundary migration textures occur only in the footwall, shear zone, or within a few hundred meters of the shear zone in the hanging wall.

[37] The Pabbar transect samples and additional samples to the northeast along the Sutlej River yields 16 subgrain rotation, 19 grain boundary migration, and six intermediate textural results. Sutlej samples are dominantly from the GHC and all show grain boundary migration, excepting a sample only ~5 m above the lithological contact (gneiss over quartzite) associated with the MCT. This sample (AW 9-22-04 (9D)) shows subgrain rotation, as does the sample immediately to the south (AW 8-17-08 (1)). Farther southwest across ~30 km,

Table 3. Thermobarometry Results

Sample Number	Temperature (°C)			Pressure (kbar)		
	Ti-In-Biotite[a]	THERMOCALC[b]	TWQ[c]	THERMOCALC	TWQ	Cor
Pabbar transect						
AW 9-19-04-(5)	541 ± 18 n = 9		520			
AW 9-19-04-(6B)	598 ± 11 n = 11		574		8.9	
AW 9-19-04-(9A)	680 ± 8 n = 8					
AW 9-19-04-(10)	678 ± 7 n = 13	620 ± 121[f]	638[f]	8.9 ± 1.9[f]	9.6[f]	0.904
AW 9-20-04-(2)	668 ± 22 n = 9					
AW 9-20-04-(3)[d]	682 ± 6 n = 9		683		7.2	
AW 9-20-04-(5)	678 ± 13 n = 12					
AW 9-20-04-(7)	638 ± 16 n = 14	669 ± 116[f]	613[f]	9.3 ± 1.7[f]	8.3[f]	0.883
AW 9-20-04-(10)	684 ± 11 n = 10		710[f]			
AW 9-21-04-(2A)	655 ± 8 n = 9		608		9.2	
AW 9-21-04-(2B)[e]	616 n = 1	617 ± 124		8.8 ± 2		0.856
AW 9-21-04-(3A)	636 ± 29 n = 9					
AW 9-22-05-(1)	618 ± 24 n = 21		639		8.7	
AW 9-22-05-(2)	676 ± 9 n = 9		665[f]			
AW 8-17-08-(1)	573 ± 10 n = 12					
AW 8-17-08-(3)	634 ± 6 n = 12					
AW 8-18-08-(2)	650 ± 21 n = 7		650			
AW 8-19-08-(7)	644 ± 18 n = 9					
AW 8-20-08-(1)	650 ± 14 n = 12					
AW 9-3-03-(12)[e]	563 n = 1	494 ± 101	545	7.2 ± 1.6	7.5	0.900
AW 9-11-03-(6)[e]	577 n = 1	446 ± 97	540	6.9 ± 1.7	8.7	0.869
AW 9-13-03-(3)[e]	564 n = 1	535 ± 116		9.6 ± 2.3		0.888
Southern Beas						
AW 9-5-03-(8)[d]	600 ± 11 n = 12					
AW 9-29-03-(10)	598 ± 27 n = 12					
AW 9-29-03-(12)[e]	586 ± 15 n = 12	480 ± 105	510	13.1 ± 2.9[g]		0.886
AW 9-29-03-(16)	573 ± 10 n = 12					
Northern Beas						
AW 9-1-04-(2)	587 ± 10 n = 11					
AW 9-1-04-(3A)	636 ± 8 n = 12					
AW 9-2-04-(2B)	579 ± 9 n = 12					
AW 9-2-04-(4)[d]	570 ± 20 n = 12					
AW 9-6-04-(2)	622 ± 9 n = 12					
AW 9-6-04-(4)[d]	569 ± 19 n = 12					
AW 9-7-04-(3)	571 ± 8 n = 12					
AW 9-8-04-(3)	580 ± 23 n = 12					
AW 9-8-04-(4B)[d]	559 ± 13 n = 11					
AW 9-8-04-(5A)[d]	569 ± 12 n = 13					
AW 9-8-04-(7)	611 ± 10 n = 10					
AW 9-10-04-(1)	666 ± 6 n = 11					

[a]Ti-In-biotite temperatures were determined by averaging calculated temperatures determined for several spot analyses within the same sample. N = number of analyzed spots.

Ti-In-biotite uncertainty is the standard deviation for all calculated temperatures for the same sample. The Ti-In-biotite geothermometer has an inherent uncertainty of ±24°C for temperatures >700°C and ±12°C for temperatures <700°C.

[b]Uncertainties for THERMOCALC are given at the 1σ level. Cor: correlation coefficient from THERMOCALC.

[c]Uncertainty of ±50°C and ±1kbar has been attributed to all TWQ data. TWQ results which do not have a corresponding P were calculated at a standard 8 kbar.

[d]Sample contains the proper assemblage for Ti-in-biotite thermometry in accordance with the *Henry et al*. [2005] paper.

[e]THERMOCALC data taken from *Webb et al*. [2011b].

[f]Garnet textures indicate that these minerals are partially resorbed (see text), so the calculated temperatures and pressures are not necessarily reflecting an equilibrium assemblage. We used data at the lowest Mn value of each garnet to estimate peak metamorphic conditions.

[g]This pressure result reflects low An content of the feldspar (An_1: outside the range of the barometer).

12 samples show grain boundary migration textures, with five scattered samples showing both grain boundary migration and subgrain rotation textures. Beyond this cluster, the next two samples to the southwest display both grain boundary migration and subgrain rotation textures, and all 10 samples farther south and west show only subgrain rotation textures.

[38] The seven samples analyzed along the southern Beas transect displayed subgrain rotation textures. The sample exposed along the core of the Pandoh syncline (AW 9-5-03 (8)) also displayed bulging recrystallization textures. Samples AW 9-29-03 (12) and AW 9-29-03 (16) contain large relict quartz grains (up to 5 mm in diameter; Figure 6D).

7. Discussion

[39] Our petrologic investigations of three areas in the Himachal Himalaya reveal spatially coherent metamorphic field gradients across amphibolite-grade and migmatitic metamorphic rocks. Along the northern Beas transect, sparse new data show that rocks record peak temperatures of ~650–780°C at low elevations to the north of ~32°10' N. Extensive results show that rocks in other positions along this transect record peak temperatures of <640°C. Rocks of the Pabbar transect dominantly record 650–700°C peak temperatures to the east of ~77°55' E, and ~450–620°C peak temperatures farther west. Similar ~450–600°C peak temperatures of the

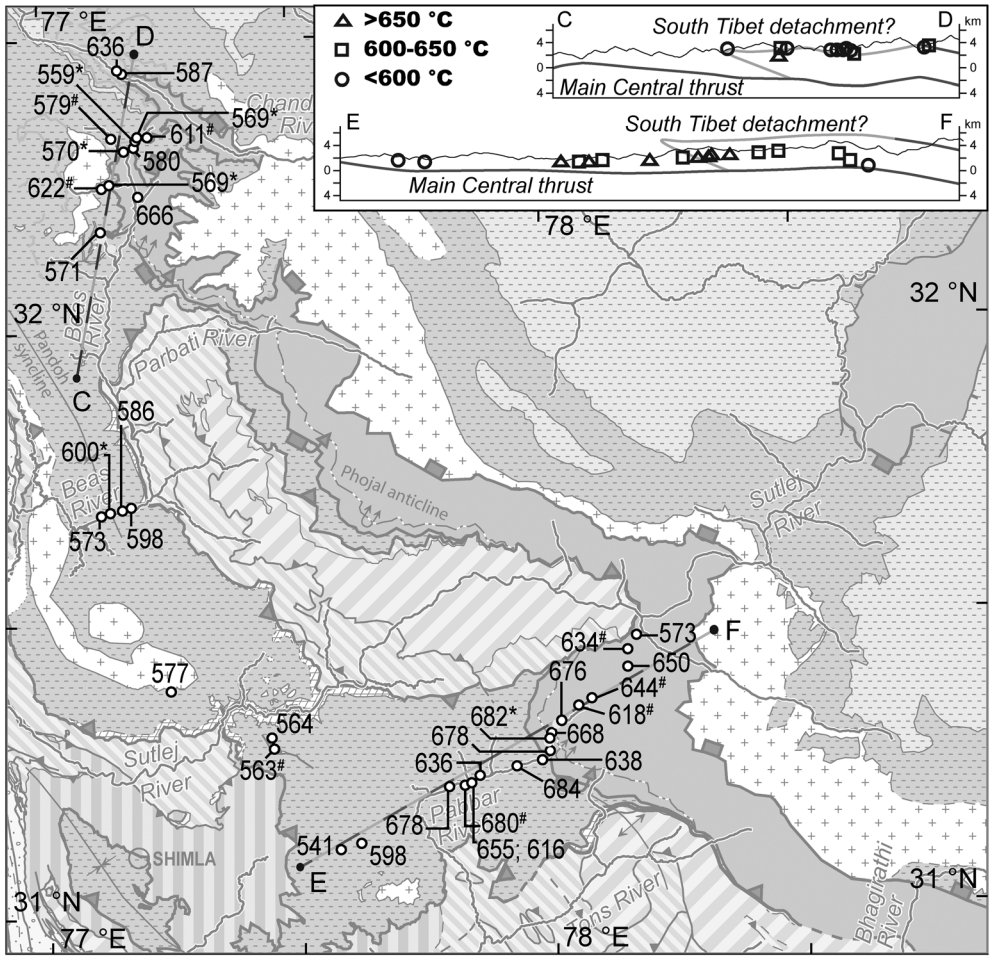

Figure 9. Regional Map (same as Figure 3) showing Ti-in-Biotite results (in °C). Results marked with a "#" indicate analyses of samples which contain graphite; results marked with "*" indicate analyses of samples with the complete calibration mineral assemblage [as defined by *Henry et al*., 2005; see text for details].

southern Beas transect record a right-way-up metamorphic field gradient, with lowest peak temperatures occurring in the core of the Pandoh syncline. Below, we compare results obtained by different methodologies, integrate our results into an updated metamorphic isograd map of the Himachal Himalaya, and discuss the implications of our findings for kinematic models for the emplacement of the GHC.

7.1. Comparison of Results Obtained via Different Pressure-Temperature Methods

[40] The variety of methods utilized in this study—i.e., petrographic analysis referenced to a petrogenetic grid, exchange and net-transfer thermobarometry, Ti-in-biotite thermometry, and analysis of quartz recrystallization textures—all yield generally consistent results with respect to peak metamorphic conditions and thermal field gradients along the three transects (Table 1 and Figures 8–10).

[41] Quartz recrystallization microstructures consistently yield lower temperatures than other methods and could be interpreted to consistently underestimate peak temperature. For example, subgrain rotation textures are commonly calibrated at 400 to 500–550°C [e.g., *Stipp et al*., 2002], but most studied samples with these textures yield temperatures of ~500 to 630°C from the other methods. The offset suggests that quartz preserves postpeak temperature deformation and/or that high strain rates increase the temperatures associated with the different quartz recrystallization mechanisms [a la *Hirth and Tullis*, 1992].

[42] Results from the petrogenetic grid and Ti-in-biotite thermometry are consistent across the northern Beas transect. If an increase of ~100°C in temperatures associated with different quartz recrystallization textures is assumed due to high strain rates, then such results are consistent with results of the other methods. All methods show the same general trends of intersample temperature gradients.

[43] Along the Pabbar transect, all methods suggest a decrease in peak metamorphic conditions from northeast to southwest, but different methods suggest that the transition from >600–650°C peak temperatures to <600–650°C peak temperatures occurs in different portions of the transect. As noted above, this transition correlates with the STD in this region [e.g., *Chambers et al*., 2009] and thus may indicate the fault presence along this transect. Ti-in-biotite thermometry suggests that this transition occurs at approximately 77°40'–77°45' E, whereas the absence of partial melts and

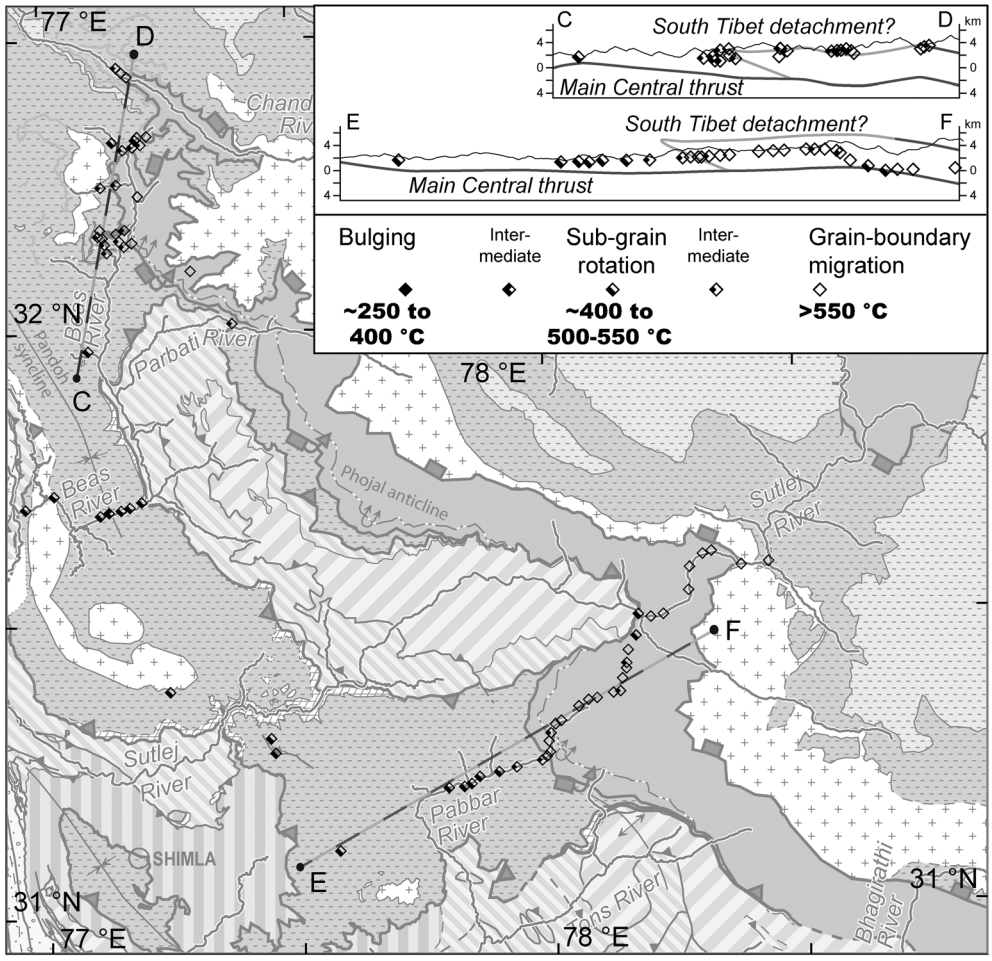

Figure 10. Regional Map (same as Figure 3) showing quartz microstructure results. Temperature ranges are given for each recrystallization mechanism. As discussed in the text, if the quartz was deformed at high strain rates, then these temperature estimates may be too low [*Hirth and Tullis*, 1992]. From a total of 73 observations, 69 are represented on the map; some sampling sites are too closely spaced to allow plotting at this scale. All results are tabulated in Supplementary File 4.

aluminosilicates, a reduction in grain size, and the transition from grain boundary migration to subgrain rotation quartz recrystallization textures suggest that this transition initiates at approximately 77°55'–78°00' E. Exchange and net-transfer reaction thermobarometric results are consistent with both patterns, because 600–650°C results were obtained from approximately 77°45' E to 77°55' E. Because none of the Ti-in-biotite samples west of 77°55' E have the calibration mineral assemblage for that method (see section 6.3), we interpret the petrographically determined transition as the best marker of the southwestward decrease in peak temperature.

[44] Results from different methods along the southern Beas transect are generally consistent, with the exception of Ti-in-biotite. Four Ti-in-biotite analyses yield temperatures of 573 to 600°C across the core of the Pandoh syncline, where all other methods indicate a temperature minimum of ~510°C or less. None of the samples analyzed via Ti-in-biotite thermometry have the calibration assemblage (see section 6.3). Constraints from the petrogenetic grid and quartz recrystallization textures both suggest a right-way-up metamorphic sequence here. The bulk of the syncline is defined by an assemblage stable at T ≈ 460–610°C, but the assemblage in the syncline core appears restricted to temperatures below ~475°C. Likewise, subgrain rotation quartz textures dominate the syncline, except in its core where lower-temperature bulging textures are also prominent. Because results other than Ti-in-biotite show a consistent pattern and the Ti-in-biotite samples lack the calibration assemblage, hereafter we do not consider the Ti-in-biotite results from this transect.

7.2. Metamorphic Field Gradients of the Himachal Himalaya

[45] The new findings help to quantify and define metamorphic field gradients which are critical for testing predictions of GHC emplacement models. Along the northern Beas transect, a new Ti-in-biotite temperature result of 666°C and phase equilibria constraints from the same sample adds to literature evidence of peak temperatures of ~650–780°C at low elevations between ~32°10' N and ~32°25' N [*Jain et al*., 1999]. Prior field mapping indicates westward and southward temperature decreases down to biotite-grade and (locally) chlorite-grade conditions [*Frank et al*., 1973, 1995; *Thöni*, 1977; *Epard et al*., 1995; *Jain et al*., 1999; *Walker et al*., 1999]. Our results here, particularly Ti-in-biotite thermometry

and quartz recrystallization textures, illustrate the initial temperature decreases down to ~500–550°C (Figures 9 and 10). Along the Pabbar transect, the southwestward decrease in peak metamorphic conditions was previously undocumented. The southern Beas transect work provides quantitative and semiquantitative evidence for decreasing peak metamorphic conditions down to ~450–510°C with increasing structural elevation, confirming the right-way-up metamorphic pattern illustrated by field mapping [*Frank et al.*, 1973, 1995; *Thöni*, 1977; *Epard et al.*, 1995].

[46] The new findings are integrated with existing regional metamorphic constraints to determine a new simplified regional metamorphic isograd map of the Himachal Himalaya and surrounding areas (Figure 11). Most existing knowledge across other parts of this region is well documented elsewhere [e.g., section 2.2.2; *Webb et al.*, 2011b: Appendix 1]. Also, two locally restricted occurrences of aluminosilicate in the MCT hanging wall to the southwest of the Kullu window are not widely considered, but are highlighted with text in Figure 11. First, sillimanite and andalusite occur in 100–500 m thick contact aureoles surrounding ~1–2 km long Late Proterozoic and/or Early Paleozoic granitic plugs in the center of the map [*Gururajan and Virdi*, 1984]. Second, *Das and Rastogi* [1988] report that a 0.5–1 km thick, discontinuous zone of sheared metapelites directly below the northern margin of the Chaur granite features an inverted metamorphic field gradient defined by index minerals, progressing from staurolite to kyanite to sillimanite. The contact between the ~830 Ma Chaur granite and underlying metasedimentary rocks is defined by a top-SW ductile shear zone that is 100 s of meters thick [*Das and Rastogi*, 1988; *Singh and Jain*, 1996; *Singh et al.*, 2002]. Such isolated occurrences may be relics of pre-Cenozoic events [e.g., *Argles et al.*, 2003].

[47] The metamorphic isograd map (Figure 11) can be directly compared to the predictions of different tectonic models as expressed by the predictive map patterns of Figure 4. The subkyanite grade conditions observed across almost the entirety of the MCT hanging wall to the southwest of the Kullu window and the right-way-up metamorphic field gradient confirmed along the southern Beas transect are inconsistent with the predictions of the pipe-planar roof and pipe-folded roof maps. Furthermore, the decrease in metamorphic grade observed south and west from the Beas River along the north Beas transect is inconsistent with the uniform high-grade conditions there shown in the pipe-planar roof map. Therefore the pipe maps, and the large-magnitude extrusion they imply, can be excluded by our findings. In contrast, the tectonic wedging and terminating STD maps are consistent with the aforementioned metamorphic field gradients, and with the overall regional pattern of metamorphism. We favor

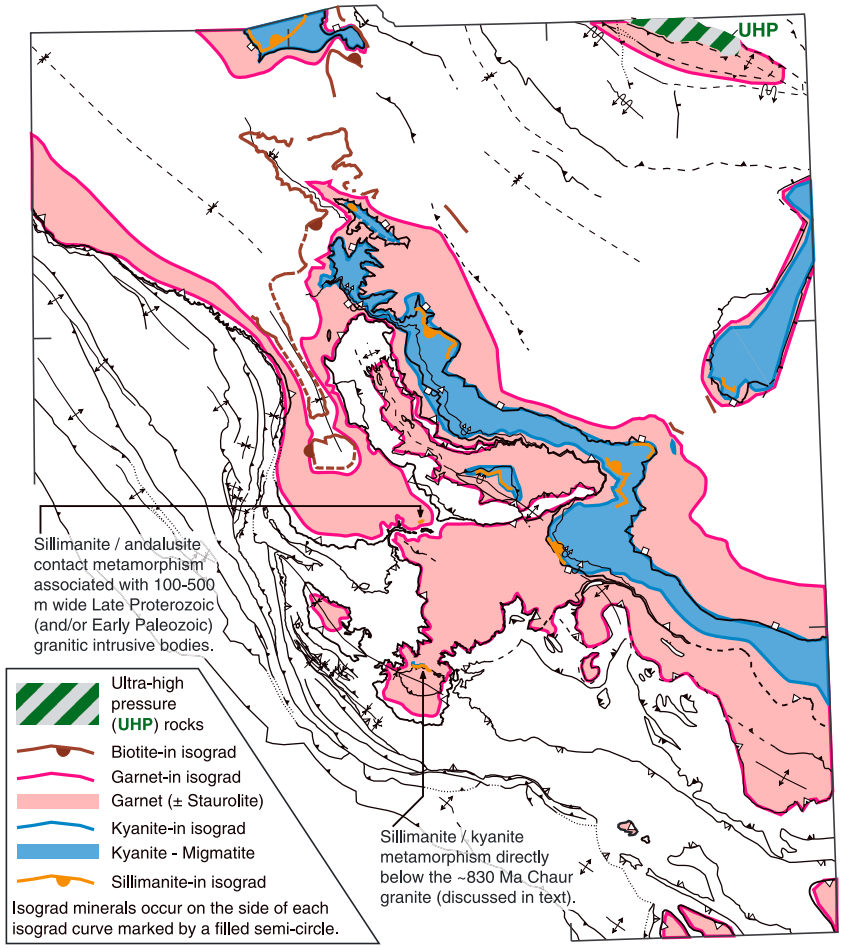

Figure 11. Metamorphic isograd map of the Himachal Himalaya, based on our work and literature sources [principally, *Frank et al.*, 1973; *Epard et al.*, 1995; *Vannay and Grasemann*, 1998] compiled in *Webb et al.* [2011b].

the tectonic wedging model because structural mapping across this area documents the STD as a ~300–600 m thick, nearly flat structure across much of the northern Beas transect that is overturned with the top-southwest Phojal anticline and can be traced farther to the southeast [*Choudhuri et al*., 1992; *Jain et al*., 1999; *Webb et al*., 2007, 2011b]. There, it appears geometrically required to either terminate in close proximity to the MCT, or merge with the MCT. It likely extends across the Pabbar transect in the zone of temperature decrease documented in this study. Existing structural work along a single trail here documented evidence of folding consistent with the Phojal anticline, but no evidence of top-northeast shear as commonly observed across the STD [*Webb et al*., 2011b]. However, outcrops along this trail were small (generally <5 m across) and commonly separated by ~1–2 km. Areal mapping of the steep but accessible surrounding area might determine the presence of top-northeast deformation here.

7.3. Emplacement of the GHC across the Whole Himalaya

[48] Because the Himachal metamorphic field gradient pattern is only consistent with tectonic wedging and terminating STD prediction maps, it strongly limits the amount of GHC extrusion possible in this portion of the Himalayan arc. The tectonic wedging model does not include extrusion. The metamorphic field gradient pattern is also consistent with a terminating STD map pattern, which in turn is compatible with wedge extrusion and channel flow models that feature a maximum of a few tens of km of extrusion [e.g., *Long and McQuarrie*, 2010].

[49] Similar findings have recently been published farther east along the orogen. *Webb et al*. [2011a] discovered a top-north shear zone bounding the frontal tip of kyanite/migmatite gneisses along the MCT in central Nepal and inferred the presence of a GHC tectonic wedging geometry there. *Kellett and Grujic* [2012] and *Corrie et al*. [2012] have both recently presented models showing GHC emplacement in the Bhutan Himalaya. These models include the same basic recognition that the GHC tapered to a southern termination between the subhorizontal STD and MCT during Early-Middle Miocene emplacement. These recent works and the new results highlight the prescience of the orogen-wide geological synthesis by *Yin* [2006], which arrives at these same conclusions, and the thermo-mechanical modeling by *Beaumont et al*. [2001], which shows similar relative motion during a postulated Eocene-Oligocene channel tunneling phase of Himalayan orogenesis.

8. Conclusions

[50] Models for a major development in the assembly of the Himalayan orogen—the emplacement of the GHC—are tested by comparing the model predictions to the metamorphic field gradients displayed across the Himachal segment of the range. New petrographic analysis referenced to a petrogenetic grid, exchange and net-transfer thermobarometry, Ti-in-biotite thermometry, and analysis of quartz recrystallization textures are used to establish and quantify the metamorphic field gradients here along three transects encircling the Kullu window of the MCT. Results reveal spatially coherent metamorphic field gradients across amphibolite-grade and migmatitic metamorphic rocks. Along the northern Beas transect, a new Ti-in-biotite temperature and phase equilibria constraints confirm literature results [from *Jain et al*., 1999] showing that rocks record peak temperatures of ~650–780°C at low elevations to the north of ~32°10' N. Rocks in other positions along this transect—i.e., at higher structural elevations, and to the south of a proposed overturned trace of the STD (at ~32°10' N)—record peak temperatures of <640°C. Rocks of the Pabbar transect dominantly record 650–700°C peak temperatures to the east of ~77°55' E, and ~450–620°C peak temperatures farther west. Peak temperatures of ~450–600°C along the southern Beas transect show a right-way-up metamorphic field gradient, with lowest peak temperatures occurring in the core of the Pandoh syncline. These results are integrated with literature data into an updated metamorphic isograd map of the Himachal Himalaya. Comparison of this map to the metamorphic isograd map pattern predictions of different models for GHC emplacement precludes models with large magnitude extrusion but permits models with modest, discontinuous extrusion. Specifically, the results exclude wedge extrusion models and channel flow-focused denudation models that include >20–30 km of extrusion of the GHC. The results are consistent with versions of these models that involve <20–30 km of GHC extrusion that is discontinuous along strike—i.e., that decreases to null across some regions, including the western Himachal Himalaya. Results are also consistent with tectonic wedging models, in which the GHC was emplaced at depth between a sole thrust and a back thrust in the Early-Middle Miocene. Constraints from previously published structural mapping [*Webb et al*., 2007, 2011b] lead us to favor the tectonic wedging hypothesis over discontinuous extrusion models.

[51] **Acknowledgments.** We thank editor Todd Ehlers, the Associate Editor, and reviewers Laurent Bollinger and Tom Argles for their careful guidance. Discussions with Dennis Donaldson, Dian He, Micah Jessup, Frank Kyte, Carrie Menold, and Bruce Yardley helped improve the manuscript. This work was supported by a start-up fund from Louisiana State University.

References

Argles, T., G., Foster, A. Whittington, N. Harris, and M. George (2003), Isotope studies reveal a complete Himalayan section in the Nanga Parbat syntaxis. *Geology*, *31*, 1109–1112, doi:10.1130/G19937.1.

Beaumont, C., R. A., Jamieson, M. H., Nguyen, and B. Lee (2001), Himalayan tectonics explained by extrusion of a low-viscosity crustal channel coupled to focused surface denudation, *Nature*, *414*, 738–742.

Beaumont, C., R. A. Jamieson, M. H. Nguyen, and S. Medvedev (2004), Crustal channel flows: 1. Numerical models with applications to the tectonics of the Himalayan-Tibetan orogen, *J. Geophys. Res.*, *109*, B06406, doi:10.1029/2003JB002809.

Berman, R. G. (2007), WinTWQ (version 2.3): a software package for performing internally-consistent thermobarometric calculations, Geological Survey of Canada, Open File 5462, (ed. 2.32), 41 pages.

Bhargava, O. N., U. K. Bassi, and R. K. Sharma (1991), The crystalline thrust sheets, age of metamorphism, evolution and mineralization of the Himachal Himalaya: Indian Minerals, 45, 1–18.

Bollinger, L., J. P. Avouac, O. Beyssac, E. J. Catlos, T. M. Harrison, M. Grove, B. Goffé, and S. Sapkota (2004), Thermal structure and exhumation history of the lesser Himalaya, *Tectonics*, TC5015, doi:10.1029/2003TC001564.

Bucher, K., and M. Frey (1994), *Petrogenesis of Metamorphic Rocks*, 7th ed., 339 pp., Springer-Verlag, Berlin, Germany.

Burchfiel, B. C., and L. H. Royden (1985), North-south extension within the convergent Himalayan region, *Geology*, *13*, 679–682.

Caddick, M. J., M. J. Bickle, N. B. W. Harris, T. J. B. Holland, M. S. A. Horstwood, R. R. Parrish, and T. Ahmad (2007), Burial and exhumation history of a Lesser Himalayan schist: Recording the formation of an inverted metamorphic sequence in NW India, *Earth Planet Sci Lett.*, *264*, 375–390, doi:10.1016/j.epsl.2007.09.011.

Célérier, J., T. M. Harrison, A. A. G. Webb, and A. Yin (2009a), The Kumaun and Garwhal Lesser Himalaya, India; Part 1, Structure and stratigraphy, *Geol. Soc. Am. Bull.*, *121*, 1262–1280, doi:10.1130/B26344.1.

Célérier, J., T. M. Harrison, O. Beyssac, F. Herman, W. J. Dunlap, and A. A. G. Webb (2009b), The Kumaun and Garwhal Lesser Himalaya, India; Part 2, Thermal and deformation histories, *Geol. Soc. Am. Bull.*, *121*, 1281–1297, doi:10.1130/B26343.1.

Chambers, J., M. Caddick, T. Argles, M. Horstwood, S. Sherlock, N. Harris, R. Parrish, and T. Ahmad (2009), Empirical constraints on extrusion mechanisms from the upper margin of an exhumed high-grade orogenic core, Sutlej valley, NW India, *Tectonophysics*, *477*, 77–92, doi:10.1016/j.tecto.2008.10.013.

Choudhuri, B. K., K. S. Bist, and B. S. Rawat (1992), Evidence for thrusting between the Higher Himalayan Crystallines and Tethyan metasediments in Lahaul and Kullu Valleys, Himachal Pradesh, *J. Himalayan Geol.*, *3*, 191–194.

Corrie, S. L., and M. J. Kohn (2011), Metamorphic history of the central Himalaya, Annapurna region, Nepal, and implications for tectonic models, *Geol. Soc. Am. Bull.*, *123*, 1863–1879, doi:10.1130/B30376.1.

Corrie, S. L., M. J. Kohn, N. McQuarrie, and S. P. Long (2012), Flattening the Bhutan Himalaya, *Earth Planet. Sci. Lett.*, *349–350*, 67–74, doi:10.1016/j.epsl.2012.07.001.

Cottle, J. M., D. J. Waters, D. Riley, O. Beyssac, and M. J. Jessup (2011). Metamorphic history of the south Tibetan Detachment System, Mt. Everst Region, Revealed by RSCM Thermometry and Phase Equilibria Modeling, *J. Metamor. Geol.*, *29*, 561–582, doi:10.1111/j.1525-1314.2011.00930.

Crouzet, C., I. Dunkl, L. Paudel, P. Arkai, T. M. Rainer, K. Balogh, and E. Appel (2007). Temperature and age constraints on the metamorphism of the Tethyan Himalaya in Central Nepal: A multidisciplinary approach, *J. Asian Earth Sci.*, *30*, 113–130, doi:10.1016/j.jseaes.2006.07.014.

Daniel, C. G., L. S. Hollister, R. R. Parrish, and D. Grujic (2003), Exhumation of the Main Central thrust from lower crustal depths, Eastern Bhutan Himalaya, *J. Metamor. Geol.*, *21*, 317–334.

Das, B. K., and R. G. Rastogi (1988), Petrology of Jutogh metapelites near Chaur, Himachal Himalaya, India, *J. Geol. Soc. India*, *31*(2), 251–266.

DiPietro, J. A., and K. R. Pogue (2004), Tectonostratigraphic subdivisions of the Himalaya: A view from the west, *Tectonics 23*, TC5001, doi:10.1029/2003TC001554.

Epard, J. L., A. Steck, J. C. Vannay, and J. Hunziker (1995), Tertiary Himalayan Structures and Metamorphism in the Kulu Valley (Mandi-Khoksar Transect of the Western Himalaya) - Shikar-Beh-Nappe and Crystalline Nappe, *Schweiz Miner. Petrog.*, *75*, 59–84.

Frank, W., G. Hoinkes, C. Miller, F. Purtscheller, W. Richter, and M. Thoni (1973), Relations between metamorphism and orogeny in a typical section of the Indian Himalayas, *Tscher. Min. Petr. Mitt.*, *20*, 303–332.

Frank, W., B. Grasemann, P. Guntli, and C. Miller (1995), Geological map of the Kishtwar-Chamba-Kulu Region (NW Himalayas, India), *Jahrb. Geol. Bundesanstalt*, *138*, 299–308.

Fuchs, G., and M. Linner (1995), Geological traverse across the western Himalaya; A contribution to the geology of eastern Ladakh, Lahul, and Chamba, *Jahrb. Geol. Bundesanstalt Wien*, *138*(4), 655–685.

Gehrels, G. E., P. G. DeCelles, A. Martin, T. P. Ojha, G. Pinhassi, and B. N. Upreti (2003), Initiation of the Himalayan Orogen as an early Paleozoic thin-skinned thrust belt, *GSA Today*, *13*(9), 4–9.

Ghent, E. D., and M. Z. Stout 1981, Geobarometry and geothermometry of plagioclase-biotite-garnet-muscovite assemblages, *Cont. Min. Pet.*, *76*, 92–97.

Godin, L., D. Grujic, R. D. Law, and M. P. Searle (2006), Channel flow, ductile extrusion and exhumation in continental collision zones: An introduction, *Geol. Soc. Lon.Spec. Pub.*, *268*, 1–23.

Grasemann, B., H. Fritz, and J. C. Vannay (1999), Quantitative kinematic flow analysis from the Main Central Thrust Zone (NW-Himalaya, India): implications for a decelerating strain path and the extrusion of orogenic wedges, *J. Struc. Geol.*, *21*, 837–853.

Grujic, D., M. Casey, C. Davidson, L. S. Hollister, R. Kundig, T. Pavlis, and S. Schmid (1996), Ductile extrusion of the Higher Himalayan Crystalline in Bhutan: Evidence form quartz microfabrics, *Tectonophys.*, *260*, 21–43.

Gururajan, N. S., and N. S. Virdi (1984), Superimposition of early Paleozoic contact metamorphism by Tertiary regional metamorphism around Dalash, District Kulu, Himachal Pradesh (India), *J. Geol. Soc. India*, *25*(8), 522–527.

Heim, A., and A. Gansser (1939), Central Himalaya geological observations of the Swiss expedition 1936: Zurich, Gebrüder Fretz, 246.

Henry, D. J., G. V. Guidotti, and J. A. Thomson (2005), The Ti-saturated surface for low-to-medium pressure metapelitic biotites: Implications for geothermometry and Ti-substitution mechanisms, *Am. Mineral.*, *90*, 316–328, doi:10.2138/am.2005.1498.

Herman, F., et al. (2010). Exhumation, crustal deformation, and thermal structure of the Nepal Himalaya derived from the inversion of thermochronological and therobarometric data and modeling of the topography, *J. Geophys. Res.*, *115*, B06407, doi:10.1029/2008JB006126.

Hirth, G.,and J. Tullis (1992), Dislocation creep regimes in quartz aggregates, *J. Struc. Geol.*, *14*, 145–160.

Hodges, K. V. (2000), Tectonics of the Himalaya and southern Tibet from two perspectives, *Geol. Soc. Am. Bull.*, *112*(3), 324–350.

Hodges, K. V., R. R. Parrish, and M. P. Searle (1996), Tectonic evolution of the central Annapurna Range, Nepalese Himalayas, *Tectonics*, *15*, 1264–1291.

Hodges, K. V., J. M. Hurtado, and K. X. Whipple (2001), Southward extrusion of Tibetan crust and its effect on Himalayan tectonics, *Tectonics*, *20*, 799–809, doi:10.1029/2001TC001281.

Holland, T. J. B., and R. Powell (1998), An internally-consistent thermodynamic dataset for phases of petrological interest, *J. Metamor. Geol.*, *16*, 309–344.

Hubbard, M. S. (1996), Ductile shear as a cause of inverted metamorphism: example from the Nepal Himalaya, *J Geol.*, *104*, 493–499.

Jain, A. K., and R. M. Manickavasagam (1993), Inverted metamorphism in the intracontinental ductile shear zone during Himalayan collision tectonics, *Geology 21*, 407–410.

Jain, A. K., R. M. Manickavasagam, and S. Singh (1999), Collision tectonics in the NW Himalaya: Deformation, metamorphism, emplacement of leucogranite along Beas-Parbati Valleys, Himachal Pradesh, *Gondwana Res. Group Mem.*, *6*, 3–37.

Jamieson, R. A., C. Beaumont, S. Medvedev, and M. H. Nguyen (2004), Crustal channel flows: 2. Numerical models with implications for metamorphism in the Himalayan-Tibetan orogen, *J. Geophys. Res.*, *109*, B06406, doi:10.1029/2003JB002811.

Jessup, M. J., J. M. Cottle, M. P. Searle, R. D. Law, R. J. Tracy, D. L. Newell, and D. J. Waters (2008), P-T-t-D paths of the Everest Series schist, Nepal, *J. Metamor. Geol.*, *26*, 717–739, doi:10.1111/j.1525-1314.2008.00784.x.

Kellett, D. A., and D. Grujic (2012), New insight into the South Tibetan detachment system: Not a single progressive deformation, *Tectonics*, *31*, TC2007, doi:10.1029/2011TC002957.

Kohn, M. J. (2008), P-T-t data from central Nepal support critical taper and repudiate large-scale channel flow of the Greater Himalayan Sequence, *Geol. Soc. Am. Bull.*, *120*, 259–273, doi:10.1130/B26252.1.

Kretz, R. (1983), Symbols of rock-forming minerals, *Am. Mineral.*, *68*, 277–279.

Langille, J. M., M. J. Jessup, J. M. Cottle, G. Lederer, and T. Ahmad (2012), Timing of metamorphism, melting and exhumation of the Leo Pargil dome, northwest India, *J. Metamor. Geol.*, doi:10.1111/j.1525-1314.2012.00998.x.

Larson, K. P., L. Godin, and R. A. Price (2010), Relationships between displacement and distortion in orogens: Linking the Himalayan foreland and hinterland in central Nepal, *Geol. Soc. Am. Bull.*, *122*, 1116–1134, doi:10.1130/B30073.1.

Law, R. D., M. J. Jessup, M. P. Searle, M. K. Francsis, D. J. Waters, and J. M. Cottle (2011), Telescoping of isotherms beneath the South Tibetan Detachment System, Mount Everest Massif, *J. Struct. Geol.*, *33*, 1569–1594, ISSN 0191-8141, doi:10.1016/j.jsg.2011.09.004.

LeFort, P. (1975), Himalayas-collided range – Present knowledge of continental arc, *J. Sci.*, *A275*, 1–44.

Le Fort, P. (1996), Evolution of the Himalaya, in The Tectonic Evolution of Asia, edited by A. Yin, and T. M. Harrison, p. 95–106, Cambridge University Press, New York.

Long, S., and N. McQuarrie (2010), Placing limits on channel flow: Insights from the Bhutan Himalaya, *Earth Planet. Sci. Lett.*, *290*, 375–390, doi:10.1016/j.epsl.2009.12.033.

Molnar, P., and P. England (1990), Temperatures, heat flux, and frictional stress near major thrust faults, *J. Geophys. Res.*, *95*, 4833–4856.

Nelson, K. D., et al. (1996), Partially molten middle crust beneath southern Tibet: Synthesis of Project INDEPTH results, *Science*, *274*, 1684–1688.

Patel, R. C., S. Singh, A. Asokan, R. M. Manickavasagam, and A. K. Jain (1993), Extensional tectonics in the Himalayan orogen, Zanskar, NW India, in Himalayan Tectonics. Geological Society Special Publication 74, edited by P. J. Treloar, and M. P. Searle, pp. 445–459, The Geological Society, London.

Reddy, S. A., M. P. Searle, and J. A. Massey (1993), Structural evolution of the High Himalayan gneiss sequence, Langtang Valley, Nepal, in Himalayan tectonics, edited by P. J. Treloar, and M. P. Searle, pp. 375–389, Geological Society Special Publication 74, London.

Richards, A., T. Argles, N. Harris, R. R. Parrish, T. Ahmad, F. Darbyshire, and E. Draganits (2005), Himalayan architecture constrained by isotopic tracers from clastic sediments, *Earth Planet. Sci. Lett.*, *236*, 773–796, doi:10.1016/j.epsl.2005.05.034.

Royden, L. H. (1993), The steady-state thermal structure of eroding orogenic belts and accretionary prisms, *J. Geophys. Res.*, *98*, 4487–4507.

Searle, M. P., and A. J. Rex (1989), Thermal model for the Zanskar Himalaya, *J. Metamorph. Geol.*, *7*, 127–134.

Searle, M. P., D. J. W. Cooper, and A. J. Rex (1988), Collision tectonics of the Ladakh - Zanskar Himalaya, *Philos. Trans. R. Soc. London*, *A326*, 117–150.

Singh, S., and A. K. Jain (1996), Ductile shearing and thrusting of the Proterozoic Chor granitoid in the Lesser Himalaya and its tectonic significance, *Global J. Geol. Soc. India*, *47*(1), 133–138.

Singh, S., M. E. Barley, S. J. Brown, A. K. Jain, and R. M. Manickavasagam (2002), SHRIMP U-Pb in zircon geochronology of the Chor granitoid: Evidence for Neoproterozoic magmatism in the Lesser Himalayan granite belt of NW India, *Precambrian Res.*, *118*, 285–292, doi:10.1016/S0301-9268(02)00107-9.

Spear, F. S. (2003), Metamorphic phase equilibria and pressure-temperature-time paths, Mineralogical Society of America, Washington D. C.

Stipp, M., H. Stünitz, R. Heilbronner, and S. M. Schmid (2002), The eastern Tonale fault zone: A "natural laboratory" for crystal plastic deformation of quartz over a temperature range from 250 to 700°C, *J. Struct. Geol.*, *24*, 1861–1884, doi:10.1016/S0191-8141(02)00035-4.

Thakur, V. C. (1998), Structure of the Chamba nappew and position of the main central thrust in Kashmir Himalaya, *J. Asian Earth Sci.*, *16*, 269–282.

Thompson, A. B. (1976), Mineral reactions in pelitic rocks: II. Calculation of some P–T–X(Fe–Mg) phase relations, *Am. J. Sci.*, *276*, 425–454.

Thöni, M. (1977), Geology, structural evolution and metamorphic zoning in the Kulu Valley (Himachal Himalayas, India) with special reference to the reversed metamorphism, *Mitt. Ges. Geol. Bergbaustud. Osterr.*, *24*, 125–187.

Vannay, J. C., and B. Grasemann (1998), Inverted metamorphism in the High Himalaya of Himachal Pradesh (NW India): Phase equilibria versus thermobarometry, *Schweiz. Mineral. Petrogr. Mitt.*, *78*, 107–132.

Vannay, J. C., Z. D. Sharp, and B. Grasemann (1999), Himalayan inverted metamorphism constrained by oxygen isotope thermometry, *Contrib. Mineral. Petrol.*, *137*(1–2), 90–101.

Vannay, J. C., and B. Grasemann (2001), Himalayan inverted metamorphism and syn-convergence extension as a consequence of a general shear extrusion, *Geol. Mag.*, *138*, 253–276.

Vannay, J. C., B. Grasemann, M. Rahn, W. Frank, A. Carter, V. Baudraz, and M. Cosca (2004), Miocene to Holocene exhumation of metamorphic crustal wedges in the NW Himalaya: Evidence for tectonic extrusion coupled to fluvial erosion, *Tectonics*, *23*, TC1014, doi:10.1029/2002TC001429.

Verma, P., S. Sengupta, D. K. Chaddha, and N. C. Pant (2005), Dehydration melting studies in a 'kyanite terrain,' Manali, NW Himalayas, *J. Asian Earth Sci.*, *25*, 345–366, doi:10.1016/j.jseaes.2004.03.005.

Walker, J. D., M. W. Martin, S. A. Bowring, M. P. Searle, D. J. Waters, and K. V. Hodges (1999), Metamorphism, melting, and extension: Age constraints from the High Himalayan Slab of southeast Zanskar and northwest Lahaul, *J. Geol.*, *107*(4), 473–495.

Webb, A. A. G., A. Yin, T. M. Harrison, J. Célérier, and W. P. Burgess (2007), The leading edge of the Greater Himalayan Crystallines revealed in the NW Indian Himalaya: Implications for the evolution of the Himalayan Orogen, *Geology*, *35*(10), 955–958, doi:10.1130/G23931A.1.

Webb, A. A. G., A. K. Schmitt, D. He, and E. L. Weigand (2011a), Structural and geochronological evidence for the leading edge of the Greater Himalayan Crystalline complex in the central Nepal Himalaya, *Earth Planet. Sci. Lett.*, *304*, 483–495, doi:10.1016/j.epsl.2011.02.024.

Webb, A. A. G., A. Yin, T. M. Harrison, J. Célérier, G. E. Gehrels, C. E. Manning, and M. Grove (2011b), Cenozoic tectonic history of the Himachal Himalaya (northwestern India) and its constraints on the formation mechanism of the Himalayan orogen, *Geosphere.*, *7*, 1013–1061, doi:10.1130/GES00627.1.

Webb, A. A. G., A. Yin, and C. S. Dubey (2013), U-Pb zircon geochronology of major lithologic units in the Eastern Himalaya: Implications for the origin and assembly of Himalayan rocks, *Geol. Soc. Am. Bull.*, *125*, 499–522, doi:10.1130/B30626.1.

Wiesmayr, G., and B. Grasemann (2002), Eohimalayan fold and thrust belt: Implications for the geodynamic evolution of the NW-Himalaya (India), *Tectonics*, *21*, 1058–17, doi:10.1029/2002TC001363.

Wyss, M. (2000), Metamorphic evolution of the northern Himachal Himalaya: Phase equilibria constraints and thermobarometry, *Schweiz. Mineral. Petrogr. Mitt.*, *80*, 317–350.

Wyss, M., J. Hermann, and A. Steck (1999), Structural and metamorphic evolution of the northern Himachal Himalaya, NW India - (Spiti-eastern Lahul-Parvati valley traverse), *Eclogae Geol. Helv.*, *92*, 3–44.

Yin, A. (2006), Cenozoic tectonic evolution of the Himalayan orogen as constrained by along-strike variation of structural geometry, exhumation history, and foreland sedimentation, *Earth Sci. Rev.*, *76*, 1–131, doi:10.1016/j.earscirev.2005.05.004.

Yin, A., C. S. Dubey, T. K. Kelty, A. A. G. Webb, T. M. Harrison, C. Y. Chou, and J. Célérier (2010), Geological correlation of the Himalayan orogen and Indian craton: Part 2. Structural geology, geochronology, and tectonic evolution of the Eastern Himalaya. *Geol. Soc. Am. Bull.*, *122*, 360–395, doi:10.1130/B26461.1.